UHASSELT
KNOWLEDGE IN ACTION

Maastricht University

Faculty of Medicine and Life Sciences
School for Life Sciences
Master of Biomedical Sciences

Master's thesis

ER-Mitochondria Crosstalk in Charcot-Marie-Tooth Type 1A

Kiara De Cauwer

Thesis presented in fulfillment of the requirements for the degree of Master of Biomedical Sciences, specialization Molecular Mechanisms in Health and Disease

SUPERVISOR :
Prof. dr. Ivo LAMBRICHTS

CO-SUPERVISOR :
Prof. dr. Esther WOLFS

MENTOR :
dr. Karen LIBBERECHT
Ms Hanne JEURISSEN

2025
2026

Transnational University Limburg is a unique collaboration of two universities in two countries: the University of Hasselt and Maastricht University.

UHASSELT
KNOWLEDGE IN ACTION

www.uhasselt.be
Universiteit Hasselt
Campus Hasselt:
Martelarenlaan 42 | 3500 Hasselt
Campus Diepenbeek:
Agoralaan Gebouw D | 3590 Diepenbeek

Faculty of Medicine and Life Sciences
School for Life Sciences
Master of Biomedical Sciences

Master's thesis

ER-Mitochondria Crosstalk in Charcot-Marie-Tooth Type 1A

Kiara De Cauwer

Thesis presented in fulfillment of the requirements for the degree of Master of Biomedical Sciences, specialization Molecular Mechanisms in Health and Disease

SUPERVISOR :
Prof. dr. Ivo LAMBRICHTS

MENTOR :
dr. Karen LIBBERECHT
Ms Hanne JEURISSEN

CO-SUPERVISOR :
Prof. dr. Esther WOLFS

ER–Mitochondria Crosstalk in Charcot-Marie-Tooth Type 1A

De Cauwer K.[1], Jeurissen H.[1], Libberecht K.[1-3], Raps T.[1] Vervliet T.[4] , Bultynck G. [4], E. Wolfs.[1] ,and Lambrichts I.[3]

[1]Laboratory for Functional Imaging & Research on Stem cells, Biomedical Research Institute (BIOMED), Universiteit Hasselt, Campus Diepenbeek, Agoralaan Gebouw C - B-3590 Diepenbeek, Belgium

[2]VIB, Center for Brain & Disease research, Laboratory of Neurobiology, Leuven, Belgium

[3]Laboratory for Histology and Regeneration (HISTOREGEN), Biomedical Research Institute (BIOMED), Universiteit Hasselt, Campus Diepenbeek, Agoralaan Gebouw C - B-3590 Diepenbeek

[4]Molecular and Cellular Signal Transduction, Department Cellular and Molecular Medicine, KU Leuven, Campus Gasthuisberg, Herestraat 49 – B-3000 Leuven, Belgium[4]

Adaptive ER-Mitochondrial Remodeling in CMT1A SCPs

To whom correspondence should be addressed: Prof. dr. I. Lambrichts. Tel:+32(0)11 26 92 45
Email: ivo.lambrichts@uhasselt.be

Keywords: CMT1A / ER stress / Mitochondria / MERCs / Schwann cell precursors

ABSTRACT

Charcot-Marie-Tooth disease (CMT) is the most common peripheral neuropathy, affecting 1 in 2500 people worldwide. CMT type 1A (CMT1A) is the most prevalent subtype and is caused by a duplication of the peripheral myelin protein 22 (PMP22) gene, which disrupts Schwann cell (SC) homeostasis. While animal models have linked this increased gene dosage to endoplasmic reticulum (ER) stress and activation of the unfolded protein response (UPR), the role of ER-mitochondrial communication and how these mechanisms manifest in human SC lineages remains unknown. This study investigates UPR signaling and introduces ER-mitochondrial crosstalk as a novel pathological feature in CMT1A, using human induced pluripotent stem cell (iPSC)-derived Schwann cell precursors (SCPs) and immature SCs (iSCs) compared to their isogenic controls. UPR activation was assessed under basal conditions and following thapsigargin-induced ER stress using qPCR and Western blot. ER–mitochondrial interactions and ultrastructure were evaluated by transmission electron microscopy, while mitochondrial organization and function were assessed using immunocytochemistry and Seahorse metabolic assays. Our data demonstrated that CMT1A SCPs showed no overt UPR dysregulation under basal and ER stress conditions, although subtle pathway-specific alterations were observed. Interestingly, UPR-related alterations became more pronounced upon maturation towards iSCs, suggesting increased proteostatic vulnerability. Additionally, despite largely preserved ER and mitochondrial ultrastructure, CMT1A SCPs exhibited increased ER–mitochondrial contact sites (MERCs) and mitofusin 2 expression, indicating altered organelle communication. Together, these findings suggest that CMT1A SCPs maintain a predominantly adaptive stress response, while altered ER–mitochondrial communication may represent an early compensatory mechanism preceding overt proteostatic dysfunction.

INTRODUCTION

Charcot-Marie-Tooth disease - Charcot-Marie-Tooth disease (CMT) is the most common peripheral neuropathy with a worldwide prevalence of 1 in 2,500 individuals (1-3). CMT is commonly characterised by progressive distal muscle weakness, muscle atrophy, and foot deformities, significantly reducing patients' quality of life (1, 2). To date, there is no cure available, and patients are completely reliant on symptomatic treatments such as physiotherapy, orthoses, and surgery for skeletal deformities, which do not address the underlying disease pathology. This highlights the need to identify novel therapeutic targets to develop disease-modifying therapies for CMT (2-4).

CMT heterogeneity - CMT represents a genetically heterogeneous group of inherited peripheral neuropathies with autosomal dominant, autosomal recessive, or X-linked inheritance patterns (1, 2). Based on genetic background, pathology, and clinical features, CMT is subdivided into several subtypes. In general, three main groups are distinguished: CMT1, CMT2, and an intermediate form. A demyelinating neuropathy with sensory impairments and muscle atrophy primarily characterizes CMT1. In contrast, CMT2 is characterized by axonal degeneration, leading to severe sensory impairment and variable muscle atrophy (1, 4). The diagnosis of CMT1 and CMT2 initially relies on electrophysiological evaluation, particularly nerve conduction velocity (NCV) measurements. In healthy individuals, NCV values vary from 50 to 70 meters/second (m/sec). In CMT1, the NCV is markedly reduced (<38 m/sec), while it remains near normal in CMT2 (>38 m/sec) (3-5). However, as CMT1 eventually leads to axonal degeneration, classification based solely on NCV findings can be challenging. Consequently, genetic testing is required to differentiate between subtypes (5).

CMT subtype 1A – CMT1A is the most frequent subtype, accounting for approximately 70% of all CMT cases. CMT1A is a demyelinating pathology of the peripheral nervous system (PNS) (1). It is caused by the duplication of a 1.4-megabase region on chromosome 17p11.2, resulting from an unequal crossover during meiosis (2, 6, 7). This region encompasses peripheral myelin protein 22 (PMP22), later identified as the disease-causing gene of CMT1A (7, 8). PMP22 is a 22-kDa intrinsic tetraspan glycoprotein, which is mainly expressed by Schwann cells (SCs), the myelin-producing cells of the PNS (7, 9). Myelin is a lipid-rich sheet surrounding axons. It ensures rapid saltatory conduction of action potentials, enabling long-distance neuronal signaling in the PNS (7-9). Although the exact function of PMP22 remains to be defined, PMP22 duplication is known to disrupt normal myelin formation and nerve conduction. Consequently, SC dysfunction is considered a key pathogenic feature of CMT1A (1, 4, 10).

Schwann cell differentiation - Beyond their role in myelin production, SCs are crucial glial cells in the PNS, supporting axonal integrity and neuronal survival (10, 11). Their ontogeny begins with the neuroectoderm-derived neural crest. These migratory cells transition into Schwann cell Precursors (SCPs) through juxtacrine signaling, specifically mediated by axon-bound Neuroregulin-1 (NRG-1) (11-13). Upon binding of NRG-1 to the ErbB2 Receptor Tyrosine Kinase/ErbB3 Receptor Tyrosine Kinase (ErbB2/ErbB3) dimer complex on SC lineages, neurogenesis is suppressed while gliogenesis is promoted, enabling axon-glial communication (11-13). During this stage, SCPs regulate nerve fasciculation, support neuronal development, and serve as progenitors of multiple peripheral cell lineages (14, 15). In late embryonic phases, SCPs differentiate into immature Schwann cells (iSCs), which will undergo radial sorting to determine their cellular fate (14, 16). This essential developmental process involves the segregation of large-caliber axons from small-caliber bundles to establish a 1:1 relationship between axons and iSCs (9, 16, 17). Terminal differentiation is ultimately dictated by axonal diameter. Large-caliber axons drive the formation of myelinating SCs, while small-caliber axons give rise to non-myelinating SCs (15-18).

Proteostasis in CMT1A – Proper protein folding and processing depend on cellular quality control mechanisms to prevent the accumulation of misfolded proteins (4, 19-22). Proteostasis encompasses the cellular pathways that regulate protein synthesis, folding, and degradation (4, 22). Within this network, the endoplasmic reticulum (ER) plays a central role by ensuring proper folding of secreted and transmembrane proteins. Correctly folded proteins are trafficked to their destinations, whereas misfolded proteins are retained within the calnexin/calreticulin (CNX/CRT) cycle for refolding or targeted for ER-associated degradation (ERAD) through retrotranslocation, ubiquitination, and

proteasomal degradation (4, 23). Sustained disruption of proteostasis can overwhelm the ERAD capacity, leading to activation of the unfolded protein response (UPR) to mitigate ER stress. The UPR comprises three parallel signaling branches: protein kinase RNA-like endoplasmic reticulum kinase (PERK), inositol-requiring enzyme 1 alpha (IRE1α), and activating transcription factor 6 (ATF6) (4, 20, 21, 24-26). Under physiological conditions, the ER chaperone binding immunoglobulin protein (BiP) binds to these stress sensors, maintaining them in an inactive state. During ER stress, BiP dissociates from the UPR stress sensors and preferentially binds misfolded proteins, thereby activating the three signaling branches to restore proteostasis (Fig. 1). **PERK** phosphorylation reduces global protein synthesis through eukaryotic initiation factor 2 alpha (eIF2α) phosphorylation while simultaneously promoting ATF4 accumulation, whereas **IRE1α** autophosphorylation induces splicing of X-box binding protein 1 (XBP1) mRNA into spliced X-box binding protein 1 (XBP1s) (4, 20, 21, 23-26). In parallel, **ATF6** translocates to the Golgi apparatus for cleavage into ATF6α, promoting the expression of cytoprotective, autophagy-related, and ERAD-associated genes. However, if ER stress remains unresolved, this adaptive response becomes maladaptive, and sustained UPR signaling activates pro-apoptotic pathways, primarily through PERK-mediated induction of C/EBP homologous protein (CHOP) (4, 20, 21, 23-26).

Mitochondrial-ER contact sites - Chronic ER stress can disrupt cellular homeostasis by impairing communication at mitochondria-ER contact sites (MERCs), also known as mitochondria-associated membranes (MAMs) (27-30). These specialized ER subdomains are tethered to the outer mitochondrial membrane (OMM) by specific protein complexes, forming a structural scaffold essential for SC function, myelination, and axonal maintenance (31-33). A primary function of MERCs is the regulation of calcium (Ca^{2+}) signaling between the ER and mitochondria (Fig. 1). Mitochondrial calcium uptake via these contact sites stimulates oxidative metabolism and adenosine triphosphate (ATP) production, linking ER signaling to mitochondrial bioenergetics (31-34). Under physiological conditions, mature SCs primarily rely on mitochondrial oxidative phosphorylation to support their myelinating and metabolic functions (35). Hence, disruption of Ca^{2+} shuttling at MERCs can impair mitochondrial homeostasis (32, 36, 37). Beyond Ca^{2+} dynamics, tethering proteins specifically, mitofusin-1 (MFN1) and mitofusin-2 (MFN2), are essential for adapting to proteotoxic stress by regulating mitochondrial fusion. Notably, MFN2 is enriched at MERCs and modulates PERK signaling, directly linking mitochondrial dynamics to the UPR (32, 38-42).

Altered proteostasis, UPR signaling, and MERCs in CMT1A – Previous studies demonstrate that PMP22 duplication disrupts proteostasis in CMT, characterizing PMP22 as an accumulation-prone secretory protein dependent on cellular quality control (4, 43-45). In CMT1A PMP22-C3 mouse models, this leads to altered UPR signaling and unresolved ER stress (44). Moreover, treatment with UPR modulator IFB-088 has been shown to alleviate ER stress and improve the demyelinating phenotype, supporting the role of proteostatic dysfunction in CMT1A pathology (44). However, the mechanisms underlying disturbed proteostasis remain incompletely understood. Furthermore, this ER dysfunction is likely to dysregulate MERCs, compromising metabolic adaptation and Ca^{2+} homeostasis (44, 46, 47). However, it remains unclear whether these findings translate to human SCs and how PMP22 overexpression drives these interconnected ER stress and MERC alterations.

Study aim - We hypothesize that PMP22 overexpression in CMT1A induces altered UPR signaling, leading to inefficient ER stress resolution that subsequently impairs MERCs, mitochondrial dynamics, and bioenergetics in human SCs. Ultimately, these alterations may represent early pathogenic mechanisms contributing to SC dysfunction. To address this hypothesis, we will use a "human-in-a-dish" model consisting of CMT1A-induced pluripotent stem cells (iPSCs) and their isogenic controls, differentiated into SCPs and iSCs. Under basal conditions and in thapsigargin-induced acute ER stress, UPR activation will be evaluated by quantitative polymerase chain reaction (qPCR) and Western blotting (WB). In parallel, ER-mitochondrial interaction and organelle ultrastructure will be assessed at basal levels using transmission electron microscopy (TEM), while mitochondrial organization and function will be analyzed by immunocytochemistry (ICC) and Seahorse metabolic assays. Together, this integrative approach aims to elucidate early pathogenic mechanisms in CMT1A SCs, potentially uncovering novel therapeutic targets within ER stress and ER-mitochondrial pathways.

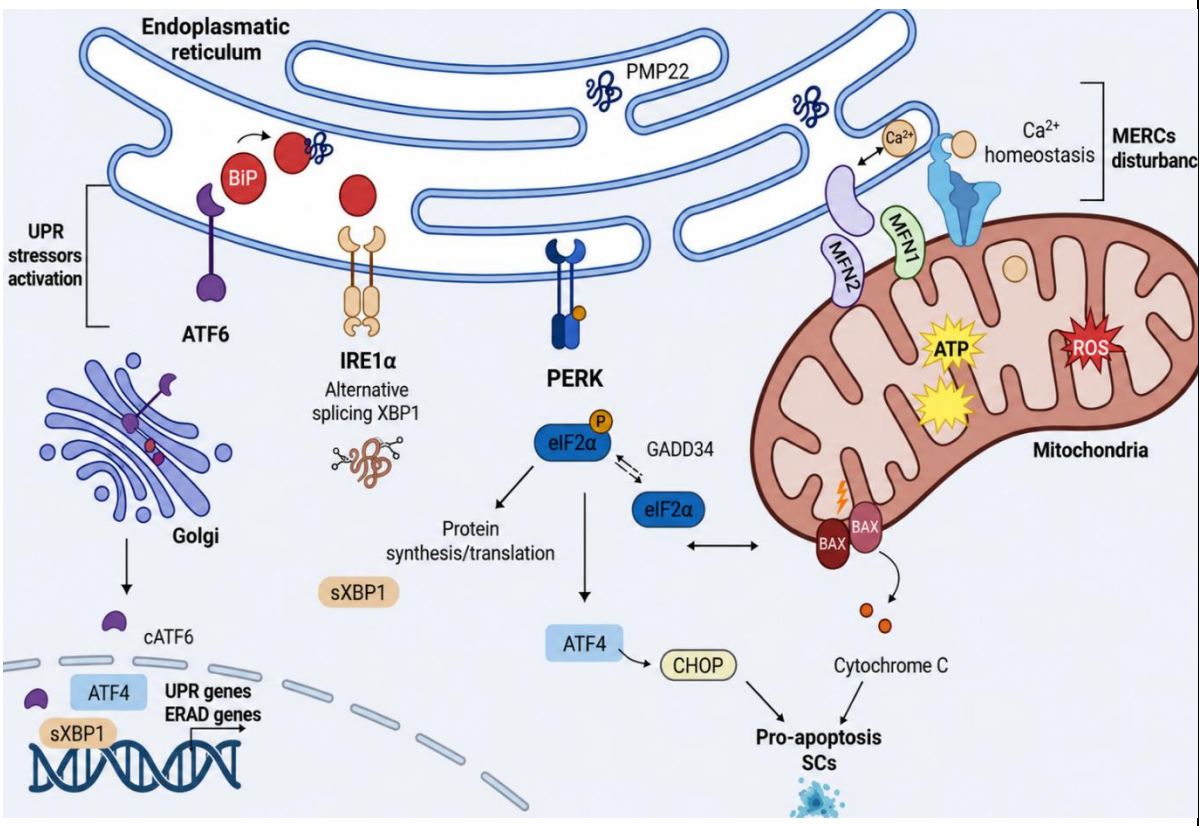

Figure 1 – ER and mitochondrial stress responses in Schwann cells in CMT1A. The accumulation of PMP22 may induce ER stress, activating the three UPR branches (PERK, IRE1α, and ATF6). Prolonged ER stress can affect ER–mitochondrial communication at MERCs, altering Ca^{2+} homeostasis, mitochondrial function, energy production, and apoptosis-associated signaling. Figure created with BioRender.com.

EXPERIMENTAL PROCEDURES

iPSC maintenance and differentiation into iPSC-derived SCPs. The CMT1A line, i267, and its isogenic control iPSC line, isogenic-i267 (ISO), were generated from fibroblasts isolated from a male CMT1A patient by the Cedars-Sinai hiPSC core facility. PMP22 duplication was confirmed by Droplet digital PCR. iPSCs were maintained and differentiated as previously described by Prior et al. (8). Briefly, iPSCs were seeded on growth factor-reduced (GFR) Matrigel-coated 6-well plates (Corning, New York, USA) in E8 flex medium (Gibco, Thermo Fisher Scientific, Waltham, Massachusetts, USA) with penicillin/ streptomycin (Pen/Strep) at a density of $1.2x10^6$ cells per well. The iPSCs were subsequently differentiated into iPSC-derived SCPs. In brief, iPSCs were cultured as single cells on GFR-Matrigel-coated-T25 flask tubes in neuronal differentiation medium consisting of a 1:1 mixture of Dulbecco's Modified Eagle Medium/Nutrient Mixture F-12 (DMEM-F12) and neurobasal culture medium (ThermoFisher Scientific), supplemented with growth factors listed in Supplementary Table 1. After 7 days, 50 ng/mL NRG-1 (PeproTech, Thermo Fisher Scientific, Waltham, MA, USA) was supplemented to promote SCP differentiation. iPSC-derived SCPs were maintained on Matrigel-GFR-coated in the appropriate medium at 37 °C in a humidified incubator with 5% CO_2 until further use. The medium was refreshed every two days. The absence of mycoplasma contamination was routinely checked.

Thapsigargin stimulation – iPSC-derived SCPs were seeded at a density of $2x10^5$ cells. A serial dilution series of 10 mM thapsigargin (AdipoGen Life Sciences, San Diego, USA) was prepared in SCP medium. Cells were treated for 1, 3, or 6 hours (h) before harvesting, depending on the experimental aim.

RNA isolation and cDNA synthesis – iPSC-derived SCPs were seeded at a density of $4x10^5$ cells and lysed at 70% confluency in 500µL Qiazol (Qiagen, Hilden, Germany). The ribonucleic acid (RNA) isolation was performed using the NZY Total RNA isolation Kit (NZYtech, Lisboa, Portugal). The resulting RNA concentration was measured using a NanoDrop™ 2000/2000c Spectrophotometer (Thermo Fisher Scientific, MA, USA). Subsequently, complementary deoxyribonucleic acid (cDNA) was synthesized using qScript cDNA SuperMix (QuantaBio, Beverly, MA, USA). Reverse transcription was performed on Bio-Rad T100™ Thermal cycler (25°C for 5 min, 42°C for 30 min, 85°C for 5 min). RNA and cDNA samples were stored at -80°C or -20°C, respectively.

Quantitative PCR reaction – A master mix containing Milli-Q, 0.3 µL of each primer (10 µM), and SYBR Green (Applied Biosystems, MA, USA) was prepared for each target gene (Supplementary Table 2). Each well of a 96-well plate was loaded with 7.5 µL master mix and 2.5 µL diluted cDNA in Milli-Q. Gene expression was normalized to the housekeeping genes Ribosomal Protein L13 (*RPL13*) and Tyrosine 3-Monooxygenase /Tryptophan 5-Monooxygenase Activation Protein Zeta (*YWHAZ*), selected based on expression stability using geNorm. No-template controls were included to assess contamination. qPCR was performed using the QuantStudio 3 RT-PCR system (Thermo Fisher Scientific).

RT-PCR – PCR reactions were performed using NZYTaq II 2x Green Master Mix (NZYTech), 0.2 µL of each primer (10 µM), and 2 µL of 1000ng cDNA in a total volume of 25 µL. Amplification was performed using Bio-Rad T100™ Thermal cycler program (94 °C for 4 min, 30 cycles (94 °C for 30 sec, 58 °C for 45 sec, 72 °C for 45 sec), and 72 °C for 10 minutes (min)). PCR products were loaded, together with a 100 base pair DNA Ladder (Invitrogen, Thermo Fisher Scientific, Spain), onto a 2.5% UltraPure agarose gel (Invitrogen) containing GelRed Nucleic Acid (1:10 000; Biotium, CA, USA). Gels were run at 200V for 70 min and visualized using the D-DiGit® Gel Scanner (LICORbio, Nebraska, USA). The integrated density was quantified using ImageQuant TL 11.0. (Cytiva,Marlborough, MA, USA) and normalized to Glyceraldehyde-3-phosphate dehydrogenase (*GAPDH*) expression (Supplementary Table 2).

W*estern blot* - iPSC-derived cells were seeded at a density of $2x10^5$ cells. Cells were lysed in filtered RIPA buffer, supplemented with protease and phosphatase inhibitors (Thermo Fisher Scientific), for 20 min on ice at 70% confluency. Lysates were mixed with 2x reducing sample buffer containing 5% β-mercaptoethanol (Merck, Darmstadt, Germany) and denatured at 95 °C for 5 min. Equal amounts of protein, based on the Bicinchoninic Acid (BCA) test (Thermofisher Scientific), were loaded onto a 12% sodium dodecyl sulfate-polyacrylamide gel together with the Precision Plus Protein™ Dual Color Standards (Bio-Rad Laboratories, Hercules, CA, USA). Electrophoresis was

performed at 100V for 10 min, followed by 150V for 70 min. Proteins were transferred onto a Polyvinylidene Fluoride (PVDF) membrane at 0.35A for 90 min. Membranes were blocked for 1 h in 3% bovine serum albumin (BSA). Blots were incubated overnight at 4 °C with primary antibodies (Supplementary Table 3). The membranes were incubated for 1 h at room temperature in the dark with HRP-conjugated secondary antibodies (Supplementary Table 3). Protein bands were detected using Pierce™ ECL Plus Western Blotting Substrate or SuperSignal™ West Pico PLUS Chemiluminescent Substrate (Thermo Fisher Scientific) and visualized using Amersham Imager 600 (Cytiva). Band-integrated intensities were analyzed using ImageQuant TL 11.0. (Cytiva), normalized to GAPDH intensity.

Immunocytochemistry – iPSC-derived SCPs were seeded onto coated coverslips at a density of 2×10^4 cells. iPSC-derived SCPs were fixed with 4% Paraformaldehyde (PFA) (Sigma-Aldrich, St. Louis, MO, USA) for 15 min. Subsequently, cells were permeabilized with 0.05% Tween 20 (Sigma-Aldrich) for 15 min. After blocking with 10% serum-free protein blocker (Dake, Agilent, Santa Clara, CA, USA) for 1 h, cells were incubated overnight at 4 °C with primary antibodies (Supplementary Table 3). The following day, cells were incubated in the dark for 1 h with secondary antibodies (1:400), followed by nuclear counterstaining with Hoechst 33342 Fluorescent Nucleic Acid Stain (1:200) (ImmunoChemistry Technologies, USA) for 20 min (Supplementary Table 3). The coverslips were mounted on Superfrost Plus Adhesion Microscope Slides (Epredia™, USA), using Fluoromount-G (Invitrogen, Carlsbad, CA, USA). Images were acquired using Nikon Eclipse Ti2-E (CFI plan-ApoChromat Lambda 20x NA 0,75), (Nikon, Japan). Fluorescence intensity was quantified by measuring the integrated density/cell using ImageJ (Fiji, NIH, Bethesda, MD, USA). Each dot represents the mean of six individual measurements from one sample. Three independent experiments were performed, each including three samples.

Seahorse XF assay – iPSC-derived SCPs were seeded in a Matrigel-coated Seahorse XF Pro M Cell Culture Microplate (Agilent Technologies) at $1x10^4$ cells. After 24 h, prior to measurement, culture medium was replaced with Seahorse XF assay medium (Agilent Technologies) supplemented with 10 mM glucose, 1 mM sodium pyruvate, 2 mM glutamine, and SCP growth factors, excluding Pen/strep (Supplementary Table 1). Mitochondrial respiration parameters, including oxygen consumption rate (OCR), basal respiration, maximal mitochondrial respiration, ATP production, proton leak, spare respiration capacity, and non-mitochondrial respiration, were assessed using the Seahorse XF Mitochondrial Stress Test. SCPs were sequentially exposed to mitochondrial inhibitors diluted in supplemented Seahorse XF assay medium: 1.5 µM oligomycin, 5 µM carbonyl cyanide-4-(trifluoromethoxy) phenylhydrazone (FCCP), and 0.5 µM rotenone/antimycin A (rot/AA). Measurements were recorded using the Agilent Seahorse XF Pro Analyzer (Agilent Technologies). Afterward, confluency was measured using the Omni Pro 12™ (Axion Biosystems, Atlanta, GA, USA). Cells were fixed with 4% PFA (Sigma-Aldrich) for 20 min and stained with Hoechst 33342 Fluorescent Nucleic Acid Stain (1:200) (ImmunoChemistry Technologies) for 15 min as additional normalization. Seahorse data points were calculated as the mean value per row, normalized to confluency.

Transmission Electron Microscopy – iPSC-derived SCPs were seeded onto coated Thermanox slides (Thermo Fisher Scientific). Cells were fixed in 2% glutaraldehyde in 0.05 M cacodylate buffer (pH 7,3) at 4 °C, followed by post-fixation in 2% Osmium tetroxide. Samples were dehydrated in graded acetone concentrations and embedded in epoxy resin (Araldite; Basel, Switzerland). Ultrathin sections (60 nm) were mounted on Formvar-coated grids and contrasted with Uranyl acetate and lead citrate. Imaging was performed using a Philips EM 208 transmission electron microscope (Philips; Eindhoven, The Netherlands) operated at 80 kV. Images were obtained at a magnification of 11.000x. Mitochondrial, ER, and MERC ultrastructure were quantified in a blinded manner using ImageJ software. Each data point represents the mean value per cell for the indicated parameter obtained from three independent experiments.

Statistics - Data were analyzed using GraphPad Prism 10.2.3. Results are presented as mean ± SEM. Normality was assessed using the Shapiro-Wilk test ($p<0,05$). Outliers were identified using Grubbs' test ($\alpha=0.05$) and excluded when justified. Statistical significance was determined using parametric or non-parametric Student's t-tests or Two-Way ANOVA, as indicated in the figure legends. Statistical significance was defined as: *$p<0.05$, **$p<0.01$, ***$p<0.001$, and ****$p<0.0001$

RESULTS

UPR integrity remains preserved in CMT1A SCPs with limited transcriptional and translational adaptations. To determine whether CMT1A SCPs exhibit altered ER stress signaling, the expression of key UPR-related genes and proteins was compared to isogenic control SCPs (Fig. 2). At the transcriptional level, a heatmap comprising genes involved in ER folding capacity, the three major UPR branches, ERAD, and apoptosis revealed no global differences between isogenic controls and CMT1A SCPs (Fig. 2A). Unexpectedly, PMP22 mRNA expression appeared non-significantly reduced in CMT1A SCPs compared to isogenic control SCPs. In addition, genes associated with ER folding capacity, including glucose-regulated protein 94 (*GRP94*), protein disulfide isomerase (*PDI*), *CRT*, and *CNX,* showed a non-significant reduction in transcriptional expression. When focusing on individual UPR branches, *BiP* and *ATF6* mRNA expression, representing the ATF6 branch, were slightly reduced in CMT1A SCPs. Additionally, *ATF4* mRNA expression was non-significantly reduced (p=0.19), whereas its downstream target *CHOP* was significantly downregulated in CMT1A SCPs (p=0.0445). In contrast, the negative feedback regulator, growth arrest and DNA damage–inducible protein 34 (GADD34), showed a non-significant increase in gene expression. Similarly, within the IRE1α pathway, *XBP1s* and *IRE1α* mRNA expression also exhibited non-significant reductions. To evaluate potential downstream consequences of ER stress, ERAD- and apoptosis-related genes were assessed. Expression of the ERAD-related gene ER degradation-enhancing α-mannosidase-like protein (*EDEM)* remained unchanged (Fig. 2A). The intrinsic mitochondrial apoptosis marker B-cell Lymphoma 2/Bcl-2–Associated X Protein (*BAX/BCL2* ratio) and the extrinsic apoptotic-related gene Fas cell surface death receptor (*FAS)* showed a non-significant increase and decrease, respectively, in CMT1A SCPs compared to isogenic controls. To determine whether these transcriptional changes were reflected at the protein level, UPR-related proteins were analyzed by WB (Fig. 2B-C). BiP protein expression was significantly increased in CMT1 SCPs (p=0.0106), whereas ATF6 protein levels showed the same downregulation observed at the transcriptional level, although not reaching significance. Consistent with the gene expression

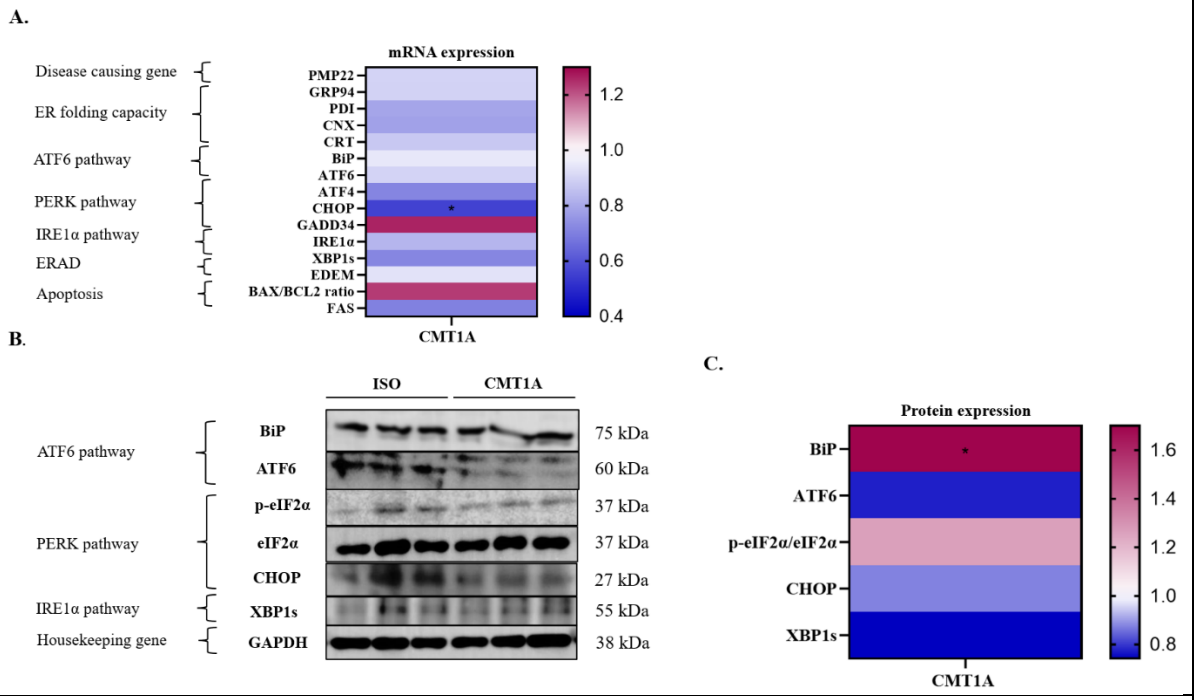

Figure 2 – UPR-related expression is largely preserved in CMT1A SCPs compared to isogenic controls at both transcriptional and translational levels, with only subtle alterations across UPR branches. A. Heatmap showing relative mRNA expression of UPR-related genes in CMT1A SCPs compared to isogenic control SCPs (n=4). **B-C**. Representative WB and analysis of UPR-related proteins (BiP, ATF6, eIF2α, p-eIF2α, CHOP, XBP1s) in CMT1A SCPs vs isogenic controls (n=3). Data are presented as mean ± SEM. Statistical analysis was performed using two-way ANOVA, followed by Tukey's multiple-comparisons test (compared with their isogenic controls). *p < 0.05.

data, PERK pathway activity, assessed by eukaryotic initiation factor 2 alpha phosphorylation (p-eIf2α/eIF2α) protein ratio, was not significantly altered. Likewise, downstream CHOP protein expression showed a non-significant decrease in CMT1A SCPs. Furthermore, XBP1s protein expression was also reduced, although not significantly (Fig. 2C). To assess the effects of an increased proteostatic burden, gene and protein expression were evaluated following high BSA (hBSA) treatment in SCPs. No overt differences were observed between isogenic controls and CMT1A SCPs following treatment. However, only a significant increase in p-eIf2α/eIF2α ratio (p<0,0001) was observed after hBSA treatment in CMT1A compared to untreated CMT1A SCPs (Supplementary Figure 1C). Additionally, UPR-related genes were also evaluated in iSCs to assess the effect of cellular maturation and its related proteostatic burden, on UPR activation (Supplementary Figure 1A). Interestingly, no differences between isogenic control iSCs and CMT1A iSCs were observed at both transcriptional and translational levels. However, cellular maturation was associated with significant increases in several UPR-related and apoptosis-related markers, particularly within the

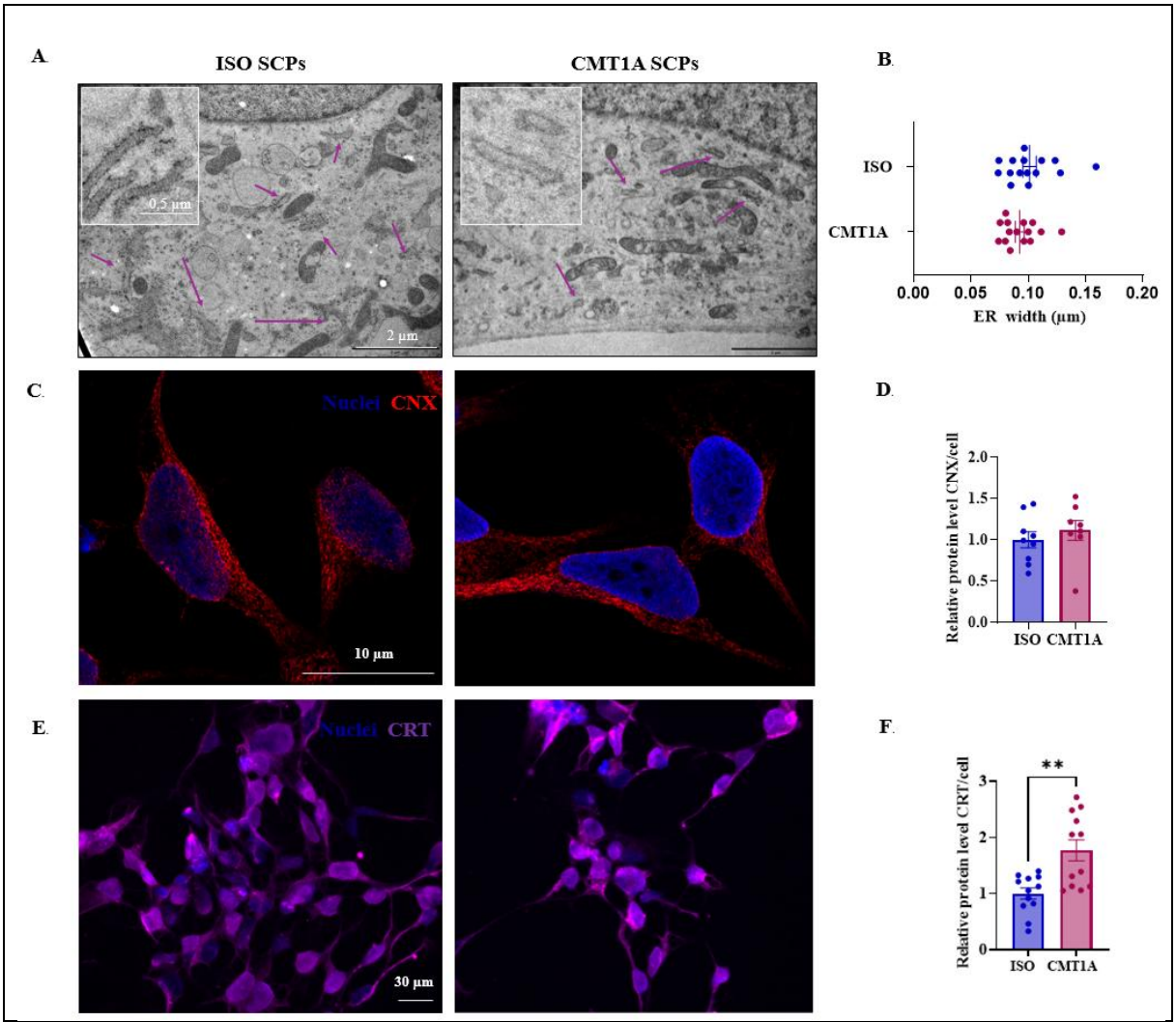

Figure 3 – The ER morphology remains unaltered in CMT1A, while CRT, an ER-resident chaperone, expression is significantly increased in CMT1A SCPs. A-B. Representative TEM images of ER ultrastructure and quantification of the ER width in isogenic control and CMT1A SCPs. Purple arrows indicate the ER. Each dot represents the mean value per cell, derived from individual measurements across three independent experiments (n=3). **C-F.** Representative fluorescent images and quantification of isogenic control and CMT1A SCPs, stained for nuclei (Hoechst, 405 nm; blue) alongside either calnexin (CNX, 555 nm; red; **C-D**) (n=3) or calreticulin (CRT, 555 nm; purple; **E-F**) (n=4). Data are presented as mean ± SEM. Statistical significance was assessed using a two-tailed unpaired Student's t-test (ER width and CNX) or a Mann–Whitney test (CRT). *p < 0.05, **p < 0.01, ***p < 0.001.

CMT1A lineage. Specifically, genes related to ER folding capacity and ATF6 signaling were significantly increased, whereas PERK pathway-related genes (*ATF4* and *CHOP*) and *XBP1s* were significantly reduced in CMT1A iSCs compared to CMT1A SCPs (Supplementary Figure 1A).

In addition, the PERK pathway was assessed at the translational level by measuring BiP and p-eIf2α/eIF2α protein levels upon maturation in CMT1A. Compared to CMT1A SCPs, the p-eIf2α/eIF2α protein expression was significantly increased in CMT1A iSCs (p=0.0004), whereas

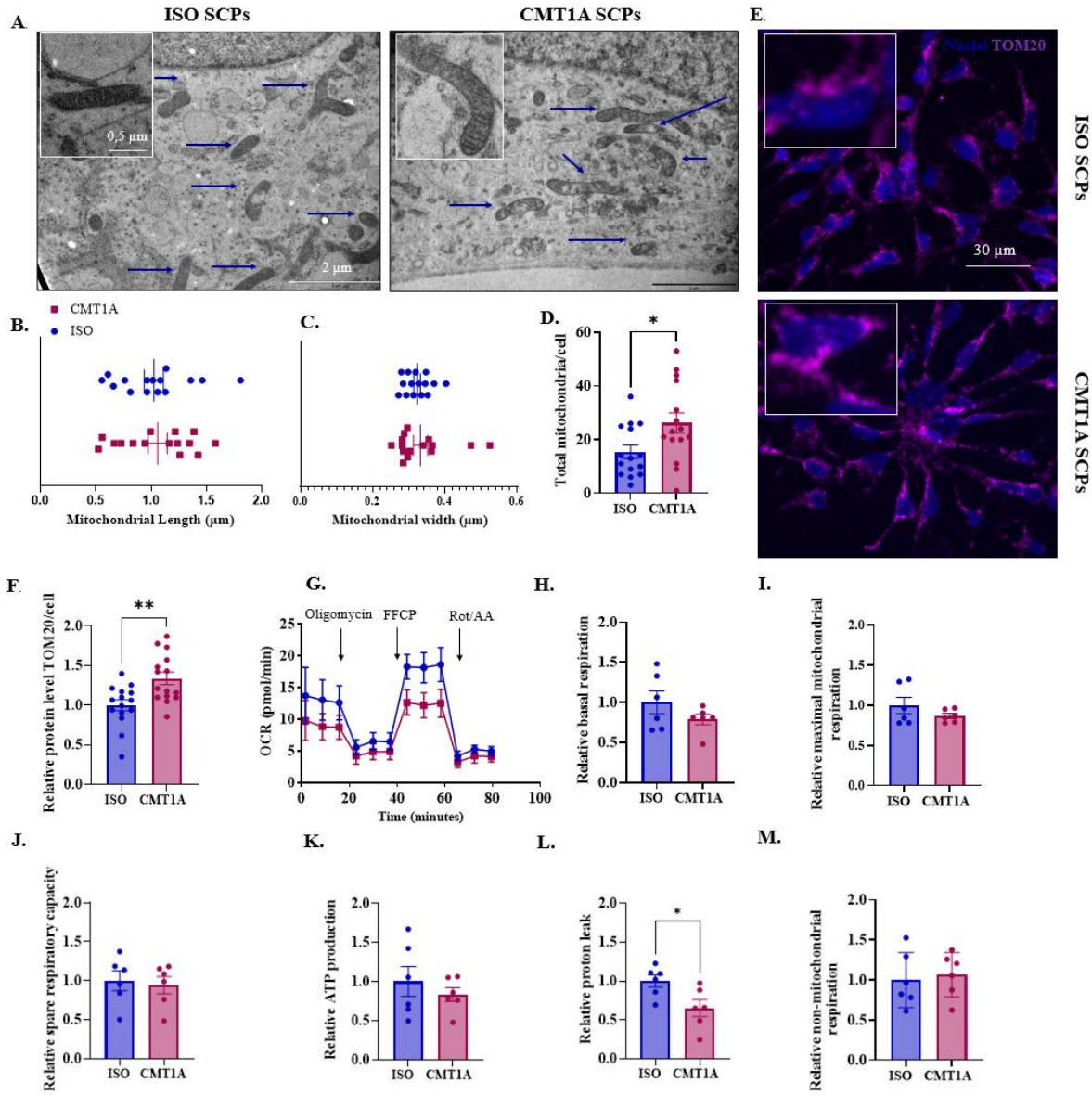

Figure 4 – The mitochondrial ultrastructure and function remain preserved, while mitochondrial abundance is significantly increased in CMT1A SCPs. A-D. Representative TEM images and quantification of the mitochondrial length (**B**), width (**C**), and total mitochondria (**D**) in isogenic control and CMT1A SCPs. Blue arrows indicate the mitochondria. Each dot represents the mean value per cell, derived from individual measurements across three independent experiments (n=3). **E-F** Representative fluorescent images, stained for nuclei (Hoechst, 405 nm; blue) and TOM20 (TOM20, 647 nm; purple), and its quantification in isogenic control and CMT1A SCPs, respectively, (n=5**). G-M**: Seahorse metabolic assays showing a representative OCR curve (**G**) and quantification of basal respiration (**H**), maximal mitochondrial respiration (**I**), spare respiratory capacity (**J**), ATP production (**K**), proton leak (**L**), and non-mitochondrial respiration (**M**) in isogenic control and CMT1A SCPs. Datapoints represent the average measurement of a single row on the Seahorse plate (n=2). Data are presented as mean ± SEM. Statistical significance was assessed using a two-tailed unpaired Student's t-test. *p < 0.05.

BiP protein expression remained unchanged (Supplementary Figure 1E). However, these maturation-associated changes in UPR-related expression were predominantly observed within the CMT1A lineage and were not detected in isogenic controls (Supplementary Figure 1A-E). Together, these transcriptional and translational data indicate that basal UPR signaling remains largely preserved in CMT1A SCPs, with only subtle pathway-specific alterations. Furthermore, UPR signaling appears to undergo adaptive remodeling upon cellular maturation towards iSCs in CMT1A.

ER morphology remained preserved, while CRT protein expression was significantly increased in CMT1A SCPs. To determine whether the preserved ER homeostasis observed in CMT1A SCPs was accompanied by maintained ER integrity, ER morphology and homeostasis were evaluated using ICC and TEM (Fig. 3). TEM analysis revealed no overt abnormalities in ER ultrastructure between isogenic control and CMT1A SCPs, as indicated by no alteration in ER width (Fig. 3A-B). To further assess ER network organization, the expression of ER-resident chaperons CNX and CRT was evaluated by ICC.

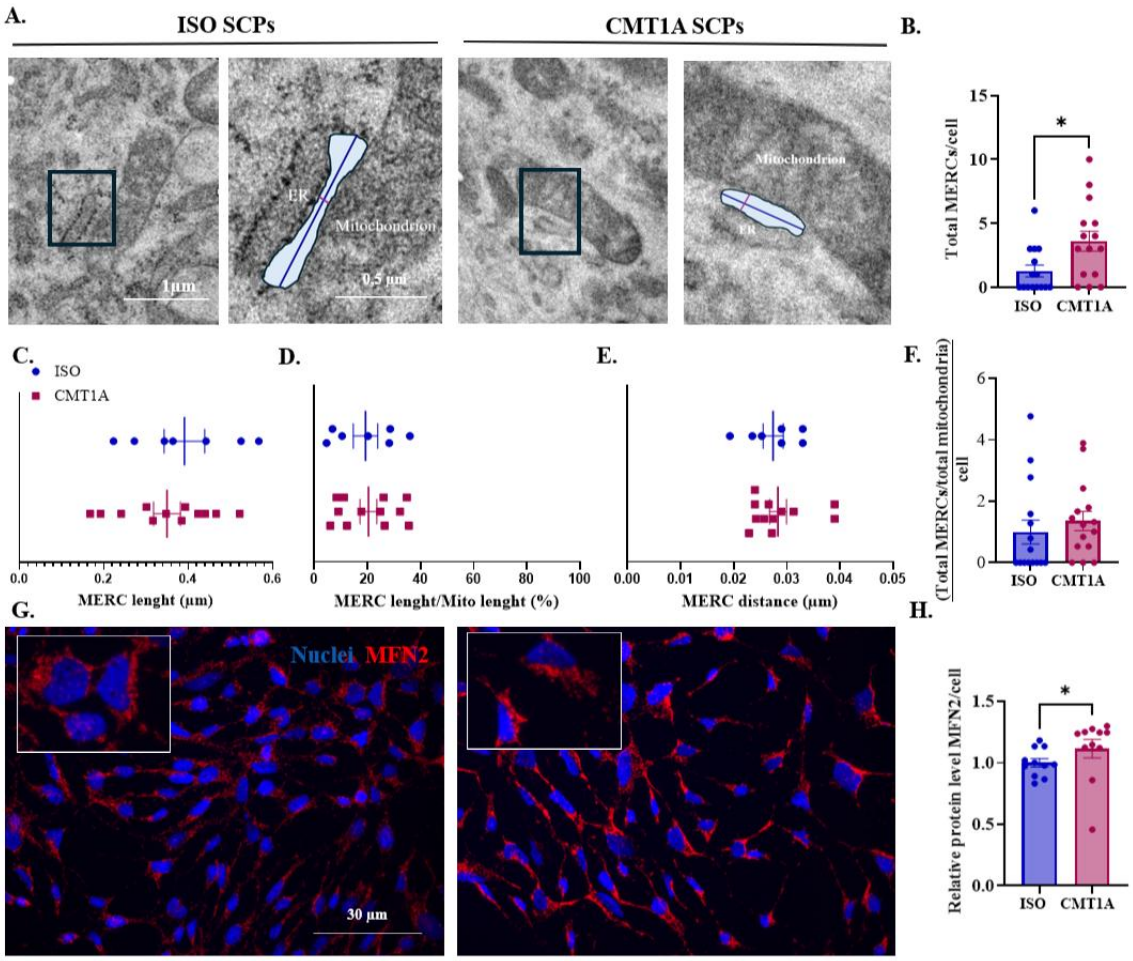

Figure 5 - The total number of ER-mitochondrial contacts is significantly increased in CMT1A SCPs, while the MERC structural organization remains preserved. A. Representative TEM images and quantification of total MERCs per cell (**B**), MERC length (**C**), MERC Coverage (**D**), MERC distance (**E**), and total MERCs/total mitochondria per cell (**F**) in isogenic control and CMT1A SCPs. The blue vertical line indicates the MERC length, while the purple horizontal line represents the MERC distance (n=3). Each dot represents the mean value per cell, derived from individual measurements across three independent experiments (n=3). **G-H.** Representative fluorescence images of isogenic control and CMT1A SCPs and quantification per cell (**H**), stained for nuclei (Hoechst, blue; 405 nm) and MFN2 (MFN2, 555 nm; red) (n=4). Data are presented as mean ± SEM. Two-tailed unpaired Student's t-test or Mann-Whitney (MERCs and MFN2) *p < 0.05, **p < 0.01, ***p < 0.001.

CNX protein expression revealed no significant differences between isogenic and CMT1A SCPs, whereas CRT expression was significantly increased (Fig. 3C-F; p=0.0068). Together, no structural changes in ER morphology were observed in CMT1A SCPs compared to their isogenic controls, while CRT protein expression was significantly increased.

While the mitochondrial ultrastructure and function remain preserved, the mitochondrial abundance was significantly increased in CMT1A SCPs. As cellular stress responses are reported to affect mitochondrial morphology and network, mitochondrial homeostasis was subsequently assessed (Fig. 4). Quantification of mitochondrial ultrastructure using TEM revealed no significant differences in mitochondrial morphology, including mitochondrial length and width, between isogenic control and CMT1A SCPs (Fig. 4A-C). However, mitochondrial abundance in each SCP was significantly increased in CMT1A following TEM analysis (Fig. 4D, p=0,0241). In addition, translocase of the Outer Mitochondrial Membrane 20 (TOM20) protein expression was evaluated by ICC as a marker for relative mitochondrial abundance in SCPs. confirming an increased mitochondrial abundance in CMT1A compared to isogenic control SCPs. (Fig. 4E-F, p=0.0030). Since mitochondrial morphology and increased abundance do not necessarily reflect mitochondrial activity, mitochondrial function and energy production were determined by Seahorse metabolic assays (Fig. 4G-M). Mitochondrial respiration was assessed by measuring OCR, basal respiration, maximal respiration, and spare respiratory capacity. Although these respiratory parameters showed reduced mitochondrial respiration in CMT1A SCPs, the differences were not significant compared with isogenic controls. Similarly, ATP-linked respiration showed a non-significant reduction in CMT1A SCPs. Interestingly, proton leak, defined as the translocation of protons from the intermembrane space back into the mitochondrial matrix independent of ATP synthase, was significantly decreased in CMT1A SCPs, whereas non-mitochondrial respiration remained unchanged (Fig. 4L, p=0.026). Together, these findings indicate that mitochondrial ultrastructure is preserved, while subtle alterations in mitochondrial respiration are present in CMT1A SCPs.

ER–mitochondria contact sites are significantly increased in CMT1A SCPs despite preserved MERC morphology. Given the close structural and functional coupling between the ER and mitochondria, TEM was performed to evaluate MERCs in CMT1A and determine whether organelle interactions were altered (Fig. 5). The total number of MERCs is significantly increased in CMT1A SCPs compared to isogenic controls (Fig. 5B, p=0,0162). In contrast, MERC length and MERC coverage relative to mitochondrial length were not altered in CMT1A SCPs (Fig. 5C-D). Furthermore, MERC distance, defined as the distance between the mitochondrial outer membrane and the ER membrane within a proximity of <0,04 µm, remained unaltered in CMT1A SCPs compared to isogenic control SCPs, with an average MERC distance of 28 nm and 27 nm, respectively (Fig. 5E). Furthermore, to account for the increased mitochondrial abundance in CMT1A SCPs, total MERCs were normalized to the total number of mitochondria per cell. This revealed a non-significant increase in MERCs per mitochondrion in CMT1A SCPs (Fig. 5F). In addition to MERC ultrastructure, MFN2, a mitochondrial outer membrane tethering protein involved in MERC interactions, protein expression was assessed by ICC, demonstrating a significantly increased expression in CMT1A SCPs (Fig. 5G-H; p=0.0336). Together, these data suggest enhanced ER-mitochondria contacts in CMT1A SCPs without major alterations in the structural organization of individual MERCs.

CMT1A SCPs respond similarly to thapsigargin-induced ER stress compared to isogenic controls. To investigate whether CMT1A SCPs respond differently to acute ER stress compared with isogenic control SCPs, ER stress was experimentally induced using thapsigargin (TG). TG is a Sarco/Endoplasmic Reticulum Ca^{2+}-ATPase (SERCA) inhibitor that disrupts ER calcium homeostasis and activates the UPR (Fig. 6A). To determine an appropriate TG concentration for downstream analyses, dose–response experiments were performed for each condition using PCR and WB (Fig. 6B-F). As an early marker of UPR activation, XBP1 splicing was assessed by PCR following 3 h stimulation with increasing concentrations of TG (Fig. 6B-C). TG treatment induced a dose-dependent increase in XBP1 splicing in both isogenic control and CMT1A SCPs compared to their respective untreated conditions, confirming effective UPR activation. However, no major differences were observed between isogenic control and CMT1A SCPs across the different TG concentrations (Fig. 6C). Remarkably, the XBP1 splicing was non-significantly upregulated in CMT1A at the basal

level (Fig. 6C). As 3 h TG stimulation revealed no significant differences between isogenic controls and CMT1A, XBP1 splicing was additionally assessed after 1 h stimulation to evaluate potential differences in early UPR response kinetics (Supplementary Figure 2A-C). No major differences in XBP1 splicing were observed between these conditions. Similarly, lower TG concentrations were included to assess the initial phase of the dose-response curve after 3 h TG stimulation (Supplementary Figure 2D-F). However, still no significant differences were observed between both conditions. In addition to XBP1 splicing, several UPR-related proteins were evaluated following 3 h TG stimulation using WB. Increasing TG concentrations induced a dose-dependent UPR response in both isogenic control and CMT1A SCPs compared to their respective basal conditions (Fig. **6**D-F). BiP protein expression increased non-significantly

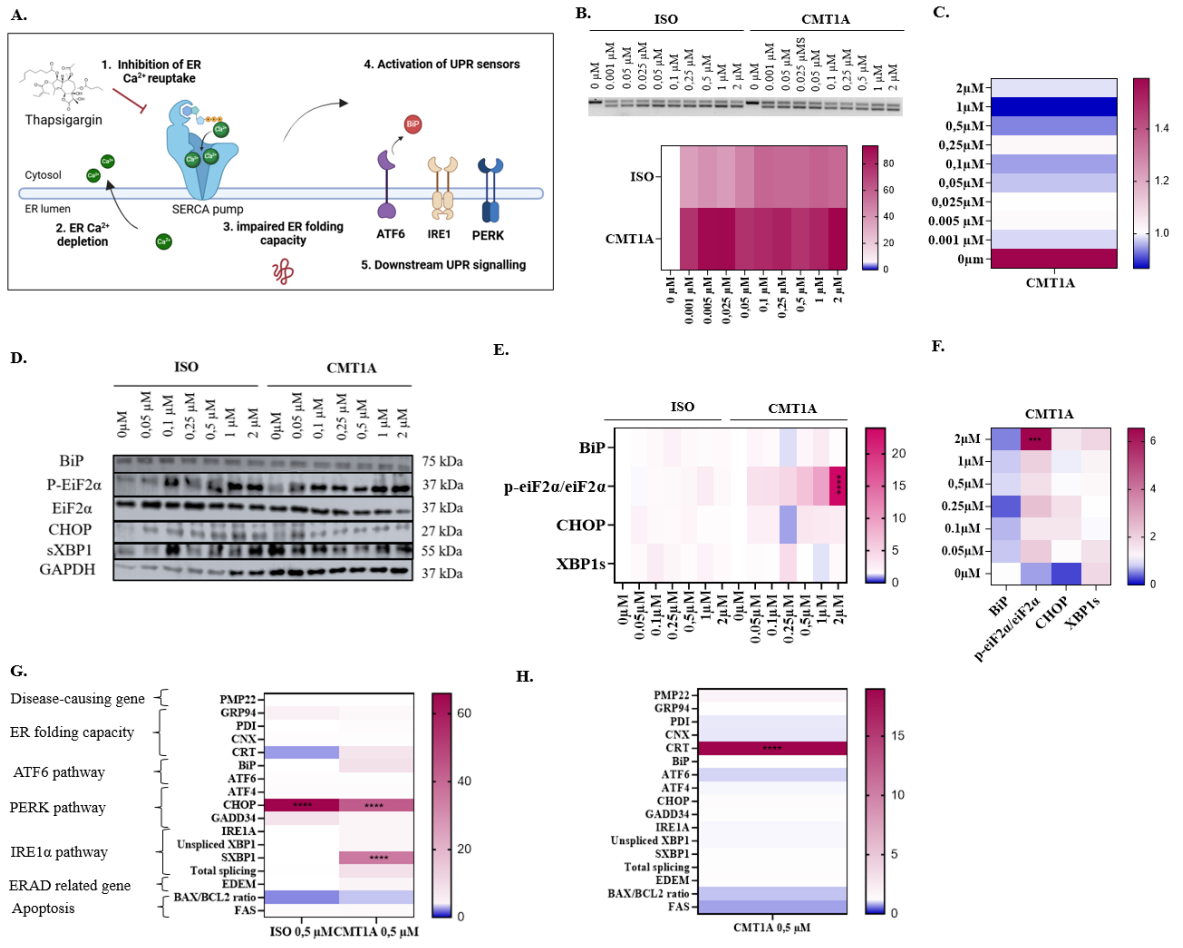

Figure 6 – CMT1A SCPs do not exhibit an altered response to experimentally induced ER stress after 3 h of thapsigargin stimulation compared with isogenic controls. A. Schematic overview of thapsigargin-induced ER-stress by inhibiting the SERCA pump and activating UPR. **B.** Representative RT-PCR image of XBP1 splicing and quantification following 3 h stimulation with increasing TG concentrations compared to the basal level 0µM (**B**) or corresponding isogenic control concentration **(C)** (n=4). **D.** Representative WB and quantification of UPR-related protein expression following 3 h stimulation with increasing TG concentrations normalized to corresponding basal levels (**E**) or corresponding isogenic control per concentration (**F)** in isogenic control and CMT1A SCPs (n=3-4). **G.** Heatmap showing the relative mRNA expression of UPR-related genes following stimulation with 0.5 µM TG in isogenic control and CMT1A SCPs compared with their respective basal conditions (**G**) or corresponding isogenic control (**H**) (n=5). Data are presented as mean ± SEM. Each dot represents the mean value per cell, derived from individual measurements across three independent experiments. Statistical analysis was performed using 2-way ANOVA with Šídák's multiple comparisons test. *p < 0.05, **p < 0.01, ***p < 0.001. Figure 6A was created with BioRender.com.

following TG-treatment in both conditions (Fig.6E). Similarly, PERK pathway-associated proteins, including the p-eIF2α/eIF2α ratio and CHOP expression, showed a gradual increase with increasing TG concentrations in both isogenic control and CMT1A SCPs compared to their basal levels. Interestingly, this increased p-eIF2α/eIF2α ratio was significant in CMT1A SCP following 2µM TG treatment compared to their basal level (Fig. 6E; p=<0,0001). Furthermore, XBP1s expression showed a non-significant increase following TG treatment in both conditions. Moreover, only a significant difference in p-eIF2α/eIF2α ratio was observed between isogenic control and CMT1A SCPs after TG treatment (Fig. 6F,p=<0,0001). To evaluate late UPR signaling, UPR-related protein levels were assessed after 6 h of TG stimulation in SCPs (Supplementary Figure 2G-I). Compared to their basal levels, only BiP expression was significantly increased in isogenic SCPs ($p<0.0001$). Moreover, the p-eIF2α/eIF2α ratio was significantly increased while CHOP expression was non-significantly decreased in CMT1A SCPs compared to their isogenic SCPs after 6 h TG stimulation (Supplementary Figure 2I, $p=0.0051$). Based on the dose–response experiments, a 3 h treatment with 0.5 µM TG was selected to evaluate the transcriptional levels of UPR-related genes under acute stress conditions, as it induced a consistent and reproducible ER stress response (Fig. 6G-H). The expression of genes associated with ER folding capacity (*GRP94* and *CNX*) and the PERK pathway (*ATF4* and *GADD34*) increased following TG treatment compared to basal conditions, although only CHOP expression reached statistical significance (Fig. 6G, $p<0001$). However, the apoptotic markers (*BAX/BCL2 ratio* and *FAS*) showed either a non-significant decrease or an increase in CMT1A SCPs, respectively. When comparing stimulated conditions, *PMP22, GRP94*, *BiP*, *CHOP*, *GADD34*, *XBP1s*, and *EDEM* expression levels were non-significantly increased in CMT1A SCPs, while *CRT* expression was significantly elevated (Fig.6H, $p<0.0001$). Conversely, *PDI, CNX*, *ATF6, ATF4, IRE1α, BAX/BCL2 ratio,* and *FAS* expression remained reduced in CMT1A SCPs compared to isogenic controls (Fig. 6H). Together, these data indicate that acute ER-stress induction elicits a comparable transcriptional and translational response in isogenic and CMT1A SCPs.

DISCUSSION

Disturbances in proteostasis and quality control systems are key drivers of several neurological disorders (29-31). SCs, the myelin-producing cells of the PNS, are particularly dependent on efficient proteostasis and organelle quality control mechanisms, including ER and mitochondrial homeostasis, due to the extensive synthesis of membrane proteins and lipids required for myelination (4). In CMT1A mouse models, PMP22 duplication has been associated with proteostatic imbalance and SC dysfunction, including altered UPR signaling *(44)*. However, the cellular consequences of PMP22-induced stress in human-derived SCs remain poorly understood. In this study, we aimed to elucidate potential differences in UPR responses and disturbances in ER-mitochondrial crosstalk in the human CMT1A model. Human iPSC-derived SCPs, obtained from a CMT1A patient and its corresponding isogenic control, were used to provide a physiologically relevant *in vitro* model to study disease-associated mechanisms in humans. Since impaired SC maturation has already been described in CMT1A models, human iPSC-derived SCPs offer the opportunity to investigate early disease-associated cellular alterations before the high proteostatic burden of mature myelinating SCs is established (4, 8, 48). To determine whether the higher proteostatic burden in SC maturation influences UPR activation in CMT1A, iSCs were included.

UPR activation in CMT1A - The UPR is activated to restore the proteostatic homeostasis following ER stress. Several studies have demonstrated that PMP22 accumulation in the ER lumen disrupts ER homeostasis, thereby inducing ER stress in SCs in CMT1A mouse models (44, 49). However, this study revealed a preserved basal UPR in CMT1A SCPs, with no overt differences in the activation of PERK, IRE1α, or ATF6 pathways compared to isogenic SCPs at either the transcriptional or translational levels. Nevertheless, BiP protein expression and CHOP gene expression showed significant differences between isogenic controls and CMT1A SCPs, indicating the importance of the PERK pathway. BiP functions as an ER chaperone and as a regulator of PERK and IRE1α activation (50). Since downstream UPR-related gene expression remained reduced in CMT1A SCPs, the increased BiP protein expression may indicate that BiP predominantly remains bound to these UPR sensors, maintaining them in an inactive state (50). Interestingly, the downstream

PERK-associated signaling appeared attenuated, as CHOP gene expression was significantly decreased, together with a reduction in ATF4 expression, in CMT1A SCPs. However, this was not reflected at the protein level. CHOP is a transcription factor that promotes apoptosis in several ways under prolonged ER stress conditions, and ATF4 regulates its expression. This downregulation may indicate the absence of chronic ER stress or reflect an adaptive mechanism that prevents progression toward terminal ER stress-induced apoptosis in CMT1A SCPs (51-53). Nevertheless, several studies confirmed that SC apoptosis appears to be limited in peripheral nerve diseases, including CMT1, even under conditions of perturbed proteostasis (4). Altogether, these data suggest that basal UPR signaling remains preserved in CMT1A SCPs, with only an attenuated downstream PERK-related apoptosis-associated signaling, indicating no sustained or maladaptive ER stress activation. Consistent with the preserved UPR, PMP22 mRNA expression was not significantly increased in CMT1A SCPs compared with isogenic controls, suggesting that PMP22-associated proteotoxic burden may remain limited at the SCP stage. This downregulation may be explained by the limited production of myelin-associated proteins in SCPs (8). Moreover, PMP22 mRNA and protein levels vary substantially among CMT1A patients, suggesting potential patient-specific effects in this model (54-56). However, as PMP22 was assessed only at the transcriptional level, no conclusions can be drawn regarding PMP22 protein accumulation in SCPs. To assess whether the limited UPR activation in CMT1A SCPs may be related to their relatively low proteostatic burden, SCPs were exposed to the carrier protein BSA. BSA, structurally similar to human serum albumin, can increase intracellular protein load, thereby challenging protein folding capacity (57, 58). Although BSA treatment appeared to increase UPR activation in both conditions, no significant differences were observed between treated isogenic control and CMT1A SCPs, supporting the overall conclusion of preserved UPR signaling in CMT1A SCPs. Another possible contributor to the limited UPR activation observed in SCPs is their developmental immaturity. SCPs are characterized as a proliferative and migratory cell type. Compared with later developmental stages, the expression of myelin-associated genes such as PMP22 and myelin protein zero (MPZ) is lower, indicating a lower proteostatic burden (17). Moreover, their proliferative and multipotent state suggests a higher adaptive and stress-resistant environment (59). Maturation towards iSCs enhances the expression of myelin-associated proteins and enhanced secretory activity, thereby increasing the demand on ER protein folding and proteostatic quality control mechanisms. Upon maturation, the expression of genes associated with ER folding capacity and UPR signaling was increased compared to the SCP stage in both conditions, suggesting an increased sensitivity to ER stress in iSCs. In contrast, downstream PERK-associated signaling, including ATF4 and CHOP expression, remained significantly reduced, consistent with the attenuated PERK-related signaling already observed in SCPs. Notably, these maturation-associated differences between iSC and SCPs were only significant in CMT1A cells. This may be attributable to higher PMP22 expression levels upon maturation in CMT1A, thereby increasing the demand on ER proteostasis. However, despite this increased proteostatic demand during maturation, no significant difference in UPR activation was observed between CMT1A iSCs and isogenic control iSCs. Moreover, these transcriptional changes remained comparable to those observed at the SCP stage. Together, these findings support that UPR signaling remains largely preserved in CMT1A at the iSC stage. Interestingly, these results did not reflect the UPR activation observed in the CMT1A PMP22-C3 mouse model by *Bai et al.* (44). A possible explanation is the differences in developmental stage between these models. The PMP22-C3 mouse model recapitulates mature myelinating SCs *in vivo* and exhibits a higher proteostatic burden due to extensive myelin production, resembling the human disease. In contrast, human iPSC-derived Schwann cell models provide insight into early human disease-associated adaptations. In addition, species- and model-specific differences between iPSCs and transgenic mouse models can contribute to these differences. Unlike human CMT1A, which is caused by a 1.4 Mb chromosomal duplication, transgenic mouse models rely on PMP22 overexpression and therefore do not fully recapitulate the genomic and epigenetic complexity of the human mutation regulation (60, 61). Importantly, both models provide novel insights into UPR pathways, aiming to elucidate the cellular mechanisms in CMT1A. Despite the preserved basal UPR signaling observed in CMT1A SCPs, it remained unclear whether CMT1A SCPs retained the

capacity to adequately respond to acute ER stress. Therefore, ER stress was experimentally induced using thapsigargin, a SERCA pump inhibitor that depletes ER Ca^{2+} and activates the UPR (62, 63). XBP1 splicing was selected as the primary readout of UPR activation due to its role as an early UPR marker (52, 64). Both isogenic control and CMT1A SCPs displayed a comparable dose-dependent increase in XBP1 splicing following TG stimulation, indicating preserved activation of the adaptive IRE1α pathway and maintenance of acute UPR responsiveness in CMT1A SCPs, as XBP1 promotes protein folding, ER-associated degradation, and the restoration of ER proteostasis (65). In addition, PERK pathway activation was observed as the p-eIF2α/eIF2α ratio and downstream ATF4 and CHOP expression were significantly increased in CMT1A SCPs, suggesting preserved activation of adaptive PERK-mediated translational attenuation following TG treatment. However, prolonged TG exposure was associated with a less pronounced CHOP response in CMT1A SCPs, consistent with the attenuated downstream PERK-associated signaling already observed under basal conditions (51, 53). This could indicate that CMT1A SCPs preferentially maintain adaptive stress responses while limiting excessive pro-apoptotic signaling under prolonged ER stress conditions. In summary, CMT1A SCPs retain the capacity to activate adaptive UPR signaling upon acute ER stress, while downstream pro-apoptotic PERK signaling may remain partially attenuated.

ER homeostasis and folding capacity in CMT1A SCPs - Given the central role of the ER in UPR signaling and protein folding, ER homeostasis and morphology were further evaluated. The ER morphology remained unaltered in CMT1A SCPs, supporting preserved ER integrity. Regarding ER folding capacity, CRT protein expression was significantly increased in CMT1A SCPs, whereas CNX expression remained unchanged. As CNX and CRT are key components of the CNX/CRT folding cycle involved in the recognition and retention of misfolded proteins, these findings suggest alterations in ER chaperone regulation rather than a global activation of ER folding capacity (66). Interestingly, as CRT is a major ER luminal Ca^{2+}-binding chaperone involved in ER Ca^{2+} buffering and the regulation of protein folding, quality control, and UPR signaling, increased CRT expression may reflect adaptive ER remodeling aimed at preserving ER proteostasis and adaptive UPR signaling in CMT1A SCPs (66-68).

Mitochondrial structure and dynamics in CMT1A SCPs - Since the close functional relationship between ER homeostasis and mitochondrial metabolism, mitochondrial morphology and bioenergetic function were subsequently evaluated. While no alterations in mitochondrial ultrastructure were observed, the mitochondrial abundance was significantly increased in CMT1A SCPs, evidenced by increased TOM20 protein expression. This increased mitochondrial abundance may reflect an adaptive mitochondrial remodeling to preserve cellular bioenergetic homeostasis, as already observed under cellular stress (69-71). Consistently, a significant increase in MFN2 expression may explain the maintenance of mitochondrial ultrastructure, as MFN2 regulates mitochondrial fusion dynamics and the maintenance of tubular mitochondrial morphology. Together, the increased mitochondrial abundance and MFN2 expression may reflect subtle alterations in mitochondrial dynamics, promoting adaptive mitochondrial remodeling in CMT1A SCPs (72-74). However, this study did not directly assess mitochondrial fusion. Despite this adaptive remodeling, Seahorse metabolic analysis did not reveal enhanced mitochondrial function in CMT1A SCPs. Interestingly, the proton leak was significantly decreased in CMT1A SCPs, suggesting reduced dissipation of the electrochemical gradient across the inner mitochondrial membrane and a more tightly coupled mitochondrial state. Increased proton leak has previously been associated with aging and several pathological conditions characterized by mitochondrial dysfunction and reduced ATP production efficiency (75, 76). However, despite the reduced proton leak, ATP production and basal respiration were not increased in CMT1A SCPs, suggesting no enhanced mitochondrial performance. Together, these findings suggest that CMT1A SCPs undergo adaptive mitochondrial remodeling, characterized by increased mitochondrial abundance and altered bioenergetic coupling, while preserving mitochondrial ultrastructure and overall function.

ER-mitochondrial crosstalk in CMT1A SCPs. ER-mitochondrial communication is primarily mediated through MERCs. As ER homeostasis and mitochondrial function remained largely preserved in CMT1A SCPs, ER-mitochondrial communication is also expected to

remain preserved. Nevertheless, the total amount of MERCs was significantly increased in CMT1A SCPs. As mitochondrial abundance was also significantly increased, this elevation may partially reflect the higher mitochondrial content observed in CMT1A SCPs rather than exclusively enhanced ER-mitochondrial coupling. However, normalization of MERCs to mitochondrial number per cell still revealed a non-significant increase in MERCs per mitochondrion in CMT1A SCPs. This suggests that the increased MERC occurrence may not be solely due to increased mitochondrial abundance. Given the involvement of MERCs in Ca^{2+} homeostasis, MERCs facilitate rapid Ca^{2+} transfer from the ER to the mitochondria through ER Inositol 1,4,5-trisphosphate receptor (IP3R) and mitochondrial voltage-dependent anion channels (VDACs) (32, 77, 78). The increased number of MERCs may facilitate this transfer between organelles, as the significant increase in CRT may support enhanced ER Ca^{2+} buffering capacity and storage (68). Although increased ER-mitochondrial coupling has previously been associated with enhanced mitochondrial Ca^{2+} uptake and respiration during adaptive stress responses, the non-significant reduction in ATP production and OCR may rather reflect adaptive alterations in ER-mitochondrial Ca^{2+} handling than enhanced mitochondrial performance in CMT1A SCPs (32, 79). Furthermore, the MERC distance is a critical contributor to this Ca^{2+} transfer efficiency. This optimal MERC distance for Ca^{2+} transfer is approximately 20 nm. On the contrary, longer MERCs (>30 nm) showed a reduction in ATP-evoked Ca^{2+} transient (30, 80). However, the observed MERC distance in CMT1A and its isogenic controls (average: 28 nm and 27 nm, respectively) lies within the distance range associated with ER-mitochondrial Ca^{2+} signaling, supporting a potential role for MERCs in ER-mitochondrial Ca^{2+} communication (80). Although these values are higher than the proposed optimal distance for maximum Ca^{2+} transport, it remains unclear whether the increased MERC formation in CMT1A-SCPs affects the efficiency of Ca^{2+} transport and its downstream functions (80). Therefore, direct functional assessment of ER-mitochondrial Ca^{2+} signaling in CMT1A SCPs is required to draw further functional conclusions. Altogether, the preserved mitochondrial ultrastructure and absence of mitochondrial dysfunction suggest that the increased MERC formation observed in CMT1A SCPs predominantly reflects adaptive rather than maladaptive ER-mitochondrial remodeling, possibly impacting Ca^{2+} signaling in CMT1A (30). Beyond Ca^{2+} signaling, MERCs are also involved in lipid metabolism, especially MERCs with narrow interorganellar distances (< 10 nm) (30). It contributes to phospholipid and triacylglycerol biosynthesis and lipid trafficking between the ER and mitochondria, regulating membrane fluidity. An increased MERC formation is hypothesized to enhance lipid metabolism and lipid exchange between the two organelles (8, 30, 81). Interestingly, previous studies showed that CMT1A SCPs demonstrated lipid dysregulation, characterized by impaired cholesterol trafficking, accumulation of polyunsaturated fatty acids in the plasma membrane, reduced membrane organization and stability, and enhanced lipid droplet biogenesis under stress conditions (8, 82). In addition, MERCs directly coordinate lipid droplet formation, linking ER lipid synthesis to storage pathways (81). This may suggest that increased MERC abundance in CMT1A SCPs not only impacts Ca^{2+} homeostasis but can also be linked to alterations in lipid metabolism in CMT1A. However, the observed MERC distance in this study was near 30 nm, which is more consistent with their involvement in Ca^{2+} signaling rather than lipid transfer. Furthermore, lipid metabolism was not assessed in this study. Therefore, further studies are required to determine the impact of MERC remodeling on lipid abnormalities in CMT1A SCPs. In addition to the potential functional consequences of MERC remodeling, altered expression of tethering proteins may contribute to this increased MERC abundance observed in CMT1A SCPs. Among these, MFN1 and 2 are OMM-associated fusogenic GTPASE proteins that regulate mitochondrial fusion dynamics (83). In particular, MFN2 is associated with MERC formation, although its exact role remains controversial. While MFN2 ablation in neuronal cells has been associated with loosening of ER-mitochondrial contacts, MFN2 overexpression has been shown to increase close ER-mitochondrial interactions and modulate the expression of MERC-associated proteins involved in Ca^{2+} signaling (42). Therefore, the significantly increased MFN2 protein expression observed in CMT1A SCPs may further support the enhanced MERC formation and adaptive ER-mitochondrial communication. However, other studies have supported an antagonistic role for MFN2 in the formation of MERCs *in vitro* (40). MFN2 mutations are the primary cause of

CMT2A and have been strongly associated with altered mitochondrial dynamics, highlighting the importance of MFN2 in peripheral nerve homeostasis (41, 83). Interestingly, MFN2 overexpression has been associated with enhanced ER-mitochondrial communication, improved mitochondrial Ca^{2+} handling, and reduced ER stress in other disease models, which is consistent with the preserved organelle homeostasis and increased MERC abundance observed in CMT1A SCPs (84, 85). Together, these findings suggest that increased MERC formation in CMT1A SCPs may reflect an adaptive response that enhances ER-mitochondrial communication while preserving overall organelle homeostasis.

UPR and MERC interaction in CMT1A. Increasing evidence indicates that adaptive UPR responses are closely linked to MERCs. Adaptive UPR signaling has recently been associated with enhanced mitochondrial function, increased mitochondrial Ca^{2+} uptake, and increased MERC formation in C. elegans and myoblast cells by Casas-Martinez JC et al. (28). This adaptive response is mediated by PERK and IRE1α activation. During ER stress, PERK localizes to MERCs and has been implicated in regulating MERC assembly, mitochondrial function, and ER-mitochondrial communication (28, 79). Interestingly, the observed increase in MERC formation in CMT1A SCPs was accompanied by an enhanced p-eIF2α/eIF2α signaling under basal conditions, which became significant following acute TG-induced ER stress. However, whether acute TG-induced ER stress further affects MERC formation remains unclear, as MERC formation was not assessed following TG stimulation. Although PERK activation was not directly assessed, these findings suggest that PERK-dependent stress responses contribute to the enhanced ER-mitochondrial coupling observed in CMT1A SCPs (28, 79). In addition, MFN2 has been implicated in both MERC regulation and is recognized as an upstream modulator of PERK signaling, further supporting a potential mechanistic link between adaptive UPR responses and ER-mitochondrial remodeling (39). However, its exact role remains controversial. Together, this may contribute to the preserved ER and mitochondrial homeostasis observed in CMT1A SCPs. However, direct functional studies are required to establish whether PERK signaling contributes to the increased MERC formation in CMT1A SCPs.

Altogether, this study revealed that CMT1A SCPs maintain a largely preserved UPR, showing only minor alterations under both basal conditions and acute thapsigargin stress. However, only attenuated downstream PERK-related apoptosis signaling was observed in CMT1A, confirming the absence of sustained or maladaptive ER stress activation. In contrast, these SCPs exhibited increased MERC formation and elevated MFN2 expression, despite preserved organelle ultrastructure. Taken together, these data suggest that adaptive ER–mitochondrial remodeling represents an early compensatory response that precedes overt cellular dysfunction in CMT1A.

Limitations and future perspectives – This study has several limitations that should be considered when interpreting our data. First, all experiments were performed in an iPSC-derived SCP disease model, representing the early developmental stage of SC lines. Although this model is relevant for investigating early disease-associated mechanisms, it does not fully recapitulate the proteostatic burden of mature myelinating SCs, present in CMT1A patients. Furthermore, it cannot be excluded that SCPs, despite carrying the confirmed CMT1A-associated PMP22 duplication, represent an early disease manifesting stage in which the full cellular consequences of this genetic defect have not yet become apparent. Nevertheless, UPR signaling was also assessed in CMT1A iSCs and their corresponding isogenic controls, further supporting the preserved proteostatic phenotype observed in this model at a more mature developmental stage. In addition, the observed alterations in MERC abundance, mitochondrial content, and proteostatic markers suggest that disease-associated cellular adaptations may already be initiated at the SCP stage despite the absence of overt cellular dysfunction. Future studies are required to validate the adaptive ER–mitochondrial remodeling identified in this study in more mature SC models and *in vivo* systems. In addition, the iPSC model was derived from a single CMT1A patient and its corresponding isogenic control. Although using an isogenic control minimizes genetic background variability, patient-specific effects cannot be excluded (86). Validation in additional patient-derived lines would therefore strengthen the generalizability of these findings. Furthermore, the impact of acute ER stress on MERC formation remains unknown, as MERCs were not assessed following thapsigargin stimulation. Moreover, the functional consequences of the observed MERC

remodeling remain speculative. Direct assessment of ER-mitochondrial Ca^{2+} transfer using calcium imaging approaches, together with functional MERC reporters, would provide important insights into the physiological relevance of the increased MERC formation observed in CMT1A SCPs. Moreover, considering the pronounced lipid dysregulation reported in CMT1A, investigating lipid metabolism and lipid trafficking may provide additional insights into the functional significance of MERC remodeling. Finally, the proposed link between PERK signaling, MFN2 expression, and MERC formation remains hypothetical. Future studies combining pharmacological modulation of PERK and MFN2 with MERC analyses will be required to establish causal relationships and determine whether adaptive ER-mitochondrial remodeling contributes to disease progression or represents a protective compensatory response in CMT1A.

CONCLUSION

This study investigated the potential differences in UPR responses and disturbances in ER-mitochondrial crosstalk in the human CMT1A SCP model. In contrast to the observed ER stress and proteostatic disturbances described in CMT1A mouse models, UPR signaling remained preserved in CMT1A SCPs under both basal conditions and acute ER stress induction. Only subtle PERK-related differences were observed in CMT1A, suggesting a role for PERK signaling in adaptive stress responses. In addition, ER and mitochondrial ultrastructure remained preserved in CMT1A SCPs. However, increased CRT, TOM20, and MFN2 expression, together with enhanced MERC formation, suggested the presence of adaptive ER-mitochondrial remodeling. Moreover, these alterations were accompanied by preserved mitochondrial function, supporting the maintenance of cellular homeostasis in CMT1A SCPs. Altogether, these findings indicate that early-stage CMT1A SCPs are characterized by preserved proteostatic homeostasis and adaptive ER-mitochondrial remodeling rather than overt cellular dysfunction.

REFERENCES

1. Murakami T, Sunada Y. Schwann Cell and the Pathogenesis of Charcot-Marie-Tooth Disease. Adv Exp Med Biol. 2019;1190:301-21.
2. Nagappa M, Sharma S, Taly AB. Charcot-Marie-Tooth Disease. StatPearls. Treasure Island (FL)2025.
3. Ma M, Li Y, Dai S, Chu M, Sun L, Liu L, Zhou JC. A meta-analysis on the prevalence of Charcot-Marie-Tooth disease and related inherited peripheral neuropathies. J Neurol. 2023;270(5):2468-82.
4. Libberecht K, Vangansewinkel T, Van Den Bosch L, Lambrichts I, Wolfs E. Proteostasis plays an important role in demyelinating Charcot Marie Tooth disease. Biochem Pharmacol. 2023;216:115760.
5. Bienfait HM, Verhamme C, van Schaik IN, Koelman JH, de Visser BW, de Haan RJ, et al. Comparison of CMT1A and CMT2: similarities and differences. J Neurol. 2006;253(12):1572-80.
6. Okamoto Y, Takashima H. The Current State of Charcot-Marie-Tooth Disease Treatment. Genes (Basel). 2023;14(7).
7. Boutary S, Echaniz-Laguna A, Adams D, Loisel-Duwattez J, Schumacher M, Massaad C, Massaad-Massade L. Treating PMP22 gene duplication-related Charcot-Marie-Tooth disease: the past, the present and the future. Transl Res. 2021;227:100-11.
8. Prior R, Silva A, Vangansewinkel T, Idkowiak J, Tharkeshwar AK, Hellings TP, et al. PMP22 duplication dysregulates lipid homeostasis and plasma membrane organization in developing human Schwann cells. Brain. 2024;147(9):3113-30.
9. Schumacher N, Vandenbosch R, Franzen R. Peripheral myelin: From development to maintenance. J Neurochem. 2025;169(1):e16268.
10. Li J, Parker B, Martyn C, Natarajan C, Guo J. The PMP22 gene and its related diseases. Mol Neurobiol. 2013;47(2):673-98.
11. Jessen KR, Mirsky R, Lloyd AC. Schwann Cells: Development and Role in Nerve Repair. Cold Spring Harb Perspect Biol. 2015;7(7):a020487.
12. Newbern J, Birchmeier C. Nrg1/ErbB signaling networks in Schwann cell development and myelination. Semin Cell Dev Biol. 2010;21(9):922-8.

13. Furlan A, Adameyko I. Schwann cell precursor: a neural crest cell in disguise? Dev Biol. 2018;444 Suppl 1:S25-S35.
14. Solovieva T, Bronner M. Schwann cell precursors: Where they come from and where they go. Cells Dev. 2021;166:203686.
15. Bosch-Queralt M, Fledrich R, Stassart RM. Schwann cell functions in peripheral nerve development and repair. Neurobiol Dis. 2023;176:105952.
16. Feltri ML, Poitelon Y, Previtali SC. How Schwann Cells Sort Axons: New Concepts. Neuroscientist. 2016;22(3):252-65.
17. Cristobal CD, Lee HK. Development of myelinating glia: An overview. Glia. 2022;70(12):2237-59.
18. Jessen KR, Mirsky R. The Success and Failure of the Schwann Cell Response to Nerve Injury. Front Cell Neurosci. 2019;13:33.
19. Libberecht K, Dirkx N, Vangansewinkel T, Vandendries W, Lambrichts I, Wolfs E. The Influence of Lysosomal Stress on Dental Pulp Stem Cell-Derived Schwann Cells. Biomolecules. 2024;14(4).
20. Lin W, Stone S. Unfolded protein response in myelin disorders. Neural Regen Res. 2020;15(4):636-45.
21. Volpi VG, Touvier T, D'Antonio M. Endoplasmic Reticulum Protein Quality Control Failure in Myelin Disorders. Front Mol Neurosci. 2016;9:162.
22. Shukla M, Narayan M. Proteostasis and Its Role in Disease Development. Cell Biochem Biophys. 2025;83(2):1725-41.
23. Oikonomou C, Hendershot LM. Disposing of misfolded ER proteins: A troubled substrate's way out of the ER. Mol Cell Endocrinol. 2020;500:110630.
24. Hetz C, Zhang K, Kaufman RJ. Mechanisms, regulation and functions of the unfolded protein response. Nat Rev Mol Cell Biol. 2020;21(8):421-38.
25. Hetz C. The unfolded protein response: controlling cell fate decisions under ER stress and beyond. Nat Rev Mol Cell Biol. 2012;13(2):89-102.
26. Chen X, Shi C, He M, Xiong S, Xia X. Endoplasmic reticulum stress: molecular mechanism and therapeutic targets. Signal Transduct Target Ther. 2023;8(1):352.
27. Kunja C, Kumar V, Kodam P, Gopu CD, Maity S. ER stress sensors at the ER-mitochondrial interface, controlling mitochondrial health in neurodegenerative diseases. Front Neurosci. 2025;19:1665272.
28. Casas-Martinez JC, Xia Q, Li P, Borja-Gonzalez M, Miranda-Vizuete A, McDermott E, et al. Adaptive ER stress promotes mitochondrial remodelling and longevity through PERK-dependent MERCS assembly. Cell Death Differ. 2026;33(4):732-47.
29. Roy R, Adhikary A, De R, Ghosh S. Mitochondria-ER crosstalk via MAMS: Bridging cellular homeostasis and cancer progression. Apoptosis. 2026;31(1):43.
30. Giacomello M, Pellegrini L. The coming of age of the mitochondria-ER contact: a matter of thickness. Cell Death Differ. 2016;23(9):1417-27.
31. Krols M, van Isterdael G, Asselbergh B, Kremer A, Lippens S, Timmerman V, Janssens S. Mitochondria-associated membranes as hubs for neurodegeneration. Acta Neuropathol. 2016;131(4):505-23.
32. Sassano ML, van Vliet AR, Agostinis P. Mitochondria-Associated Membranes As Networking Platforms and Regulators of Cancer Cell Fate. Front Oncol. 2017;7:174.
33. Bui V, Santerre M, Shcherbik N, Sawaya BE. Mitochondria-associated membranes (MAMs): molecular organization, cellular functions, and their role in health and disease. FEBS Open Bio. 2026;16(1):11-24.
34. Luan Y, Luan Y, Yuan RX, Feng Q, Chen X, Yang Y. Structure and Function of Mitochondria-Associated Endoplasmic Reticulum Membranes (MAMs) and Their Role in Cardiovascular Diseases. Oxid Med Cell Longev. 2021;2021:4578809.
35. Ino D, Iino M. Schwann cell mitochondria as key regulators in the development and maintenance of peripheral nerve axons. Cell Mol Life Sci. 2017;74(5):827-35.
36. Follis R, Prabhu VV, Carter BD. The Influence of Schwann Cell Metabolism and Dysfunction on Axon Maintenance. Glia. 2025;73(12):2338-52.

37. Liberti MV, Locasale JW. The Warburg Effect: How Does it Benefit Cancer Cells? Trends Biochem Sci. 2016;41(3):211-8.
38. Wilson EL, Metzakopian E. ER-mitochondria contact sites in neurodegeneration: genetic screening approaches to investigate novel disease mechanisms. Cell Death Differ. 2021;28(6):1804-21.
39. Cao Y, Chen Z, Hu J, Feng J, Zhu Z, Fan Y, et al. Mfn2 Regulates High Glucose-Induced MAMs Dysfunction and Apoptosis in Podocytes via PERK Pathway. Front Cell Dev Biol. 2021;9:769213.
40. Filadi R, Greotti E, Turacchio G, Luini A, Pozzan T, Pizzo P. Mitofusin 2 ablation increases endoplasmic reticulum-mitochondria coupling. Proc Natl Acad Sci U S A. 2015;112(17):E2174-81.
41. Feely SM, Laura M, Siskind CE, Sottile S, Davis M, Gibbons VS, et al. MFN2 mutations cause severe phenotypes in most patients with CMT2A. Neurology. 2011;76(20):1690-6.
42. Han S, Zhao F, Hsia J, Ma X, Liu Y, Torres S, et al. The role of Mfn2 in the structure and function of endoplasmic reticulum-mitochondrial tethering in vivo. J Cell Sci. 2021;134(13).
43. Chittoor VG, Sooyeon L, Rangaraju S, Nicks JR, Schmidt JT, Madorsky I, et al. Biochemical characterization of protein quality control mechanisms during disease progression in the C22 mouse model of CMT1A. ASN Neuro. 2013;5(5):e00128.
44. Bai Y, Treins C, Volpi VG, Scapin C, Ferri C, Mastrangelo R, et al. Treatment with IFB-088 Improves Neuropathy in CMT1A and CMT1B Mice. Mol Neurobiol. 2022;59(7):4159-78.
45. Lee S, Bazick H, Chittoor-Vinod V, Al Salihi MO, Xia G, Notterpek L. Elevated Peripheral Myelin Protein 22, Reduced Mitotic Potential, and Proteasome Impairment in Dermal Fibroblasts from Charcot-Marie-Tooth Disease Type 1A Patients. Am J Pathol. 2018;188(3):728-38.
46. Zhao WB, Sheng R. The correlation between mitochondria-associated endoplasmic reticulum membranes (MAMs) and Ca(2+) transport in the pathogenesis of diseases. Acta Pharmacol Sin. 2025;46(2):271-91.
47. Zhao C, Liao Y, Rahaman A, Kumar V. Towards Understanding the Relationship Between ER Stress and Unfolded Protein Response in Amyotrophic Lateral Sclerosis. Front Aging Neurosci. 2022;14:892518.
48. Van Lent J, Prior R, Perez Siles G, Cutrupi AN, Kennerson ML, Vangansewinkel T, et al. Advances and challenges in modeling inherited peripheral neuropathies using iPSCs. Exp Mol Med. 2024;56(6):1348-64.
49. Okamoto Y, Pehlivan D, Wiszniewski W, Beck CR, Snipes GJ, Lupski JR, Khajavi M. Curcumin facilitates a transitory cellular stress response in Trembler-J mice. Hum Mol Genet. 2013;22(23):4698-705.
50. Kopp MC, Larburu N, Durairaj V, Adams CJ, Ali MMU. UPR proteins IRE1 and PERK switch BiP from chaperone to ER stress sensor. Nat Struct Mol Biol. 2019;26(11):1053-62.
51. Rozpedek W, Pytel D, Mucha B, Leszczynska H, Diehl JA, Majsterek I. The Role of the PERK/eIF2alpha/ATF4/CHOP Signaling Pathway in Tumor Progression During Endoplasmic Reticulum Stress. Curr Mol Med. 2016;16(6):533-44.
52. Hetz C, Martinon F, Rodriguez D, Glimcher LH. The unfolded protein response: integrating stress signals through the stress sensor IRE1alpha. Physiol Rev. 2011;91(4):1219-43.
53. Novoa I, Zeng H, Harding HP, Ron D. Feedback inhibition of the unfolded protein response by GADD34-mediated dephosphorylation of eIF2alpha. J Cell Biol. 2001;153(5):1011-22.
54. Pantera H, Shy ME, Svaren J. Regulating PMP22 expression as a dosage sensitive neuropathy gene. Brain Res. 2020;1726:146491.
55. Katona I, Wu X, Feely SM, Sottile S, Siskind CE, Miller LJ, et al. PMP22 expression in dermal nerve myelin from patients with CMT1A. Brain. 2009;132(Pt 7):1734-40.
56. Serfecz J, Bazick H, Al Salihi MO, Turner P, Fields C, Cruz P, et al. Downregulation of the human peripheral myelin protein 22 gene by miR-29a in cellular models of Charcot-Marie-Tooth disease. Gene Ther. 2019;26(12):455-64.
57. Adamczyk O, Szota M, Rakowski K, Prochownik M, Doveiko D, Chen Y, Jachimska B. Bovine Serum Albumin as a Platform for Designing Biologically Active Nanocarriers-Experimental and Computational Studies. Int J Mol Sci. 2023;25(1).
58. Chou MJ, Yu HY, Hsia JC, Chen YH, Hung TT, Chao HM, et al. Highly Efficient Intracellular Protein Delivery by Cationic Polyethyleneimine-Modified Gelatin Nanoparticles. Materials (Basel). 2018;11(2).

59. Jessen KR, Mirsky R. Schwann Cell Precursors; Multipotent Glial Cells in Embryonic Nerves. Front Mol Neurosci. 2019;12:69.
60. Taruta A, Matsumoto SI, Masuda Y, Hiyoshi T, Harada A, Kosugi Y, Nakashima M. Characterization of a humanized mouse model of Charcot-Marie-Tooth type 1A for the discovery of human PMP22-targeting drugs. Front Neurol. 2025;16:1658204.
61. Fridman V, Saporta MA. Mechanisms and Treatments in Demyelinating CMT. Neurotherapeutics. 2021;18(4):2236-68.
62. Lindner P, Christensen SB, Nissen P, Moller JV, Engedal N. Cell death induced by the ER stressor thapsigargin involves death receptor 5, a non-autophagic function of MAP1LC3B, and distinct contributions from unfolded protein response components. Cell Commun Signal. 2020;18(1):12.
63. Zhu Y, Burg T, Neyrinck K, Vervliet T, Nami F, Vervoort E, et al. Correction to: Disruption of MAM integrity in mutant FUS oligodendroglial progenitors from hiPSCs. Acta Neuropathol. 2024;147(1):99.
64. He Y, Sun S, Sha H, Liu Z, Yang L, Xue Z, et al. Emerging roles for XBP1, a sUPeR transcription factor. Gene Expr. 2010;15(1):13-25.
65. Touvier T, Veneri FA, Claessens A, Ferri C, Mastrangelo R, Sorgiati N, et al. Activation of XBP1s attenuates disease severity in models of proteotoxic Charcot-Marie-Tooth type 1B. Brain. 2025;148(6):1978-93.
66. Kozlov G, Gehring K. Calnexin cycle - structural features of the ER chaperone system. FEBS J. 2020;287(20):4322-40.
67. Nguyen DT, Le TM, Hattori T, Takarada-Iemata M, Ishii H, Roboon J, et al. The ATF6beta-calreticulin axis promotes neuronal survival under endoplasmic reticulum stress and excitotoxicity. Sci Rep. 2021;11(1):13086.
68. Michalak M. Calreticulin: Endoplasmic reticulum Ca(2+) gatekeeper. J Cell Mol Med. 2024;28(5):e17839.
69. Sanfrancesco VC, Della Mea D, Hood DA. Unfolding Resilience: Molecular Integration of the Integrated Stress Response and Mitochondrial UPR in Skeletal Muscle Homeostasis. Muscles. 2026;5(2).
70. Wen H, Deng H, Li B, Chen J, Zhu J, Zhang X, et al. Mitochondrial diseases: from molecular mechanisms to therapeutic advances. Signal Transduct Target Ther. 2025;10(1):9.
71. Jagtap YA, Kumar P, Kinger S, Dubey AR, Choudhary A, Gutti RK, et al. Disturb mitochondrial associated proteostasis: Neurodegeneration and imperfect ageing. Front Cell Dev Biol. 2023;11:1146564.
72. Codron P, Chevrollier A, Kane MS, Echaniz-Laguna A, Latour P, Reynier P, et al. Increased mitochondrial fusion in a autosomal recessive CMT2A family with mitochondrial GTPase mitofusin 2 mutations. J Peripher Nerv Syst. 2016;21(4):365-9.
73. Schiavon CR, Shadel GS, Manor U. Impaired Mitochondrial Mobility in Charcot-Marie-Tooth Disease. Front Cell Dev Biol. 2021;9:624823.
74. Amiott EA, Lott P, Soto J, Kang PB, McCaffery JM, DiMauro S, et al. Mitochondrial fusion and function in Charcot-Marie-Tooth type 2A patient fibroblasts with mitofusin 2 mutations. Exp Neurol. 2008;211(1):115-27.
75. Zhang H, Alder NN, Wang W, Szeto H, Marcinek DJ, Rabinovitch PS. Reduction of elevated proton leak rejuvenates mitochondria in the aged cardiomyocyte. Elife. 2020;9.
76. Ardalan A, Smith MD, Jelokhani-Niaraki M. Uncoupling Proteins and Regulated Proton Leak in Mitochondria. Int J Mol Sci. 2022;23(3).
77. Morciano G, Marchi S, Morganti C, Sbano L, Bittremieux M, Kerkhofs M, et al. Role of Mitochondria-Associated ER Membranes in Calcium Regulation in Cancer-Specific Settings. Neoplasia. 2018;20(5):510-23.
78. Ferrari D, Pinton P, Campanella M, Callegari MG, Pizzirani C, Rimessi A, et al. Functional and structural alterations in the endoplasmic reticulum and mitochondria during apoptosis triggered by C2-ceramide and CD95/APO-1/FAS receptor stimulation. Biochem Biophys Res Commun. 2010;391(1):575-81.
79. Bravo R, Vicencio JM, Parra V, Troncoso R, Munoz JP, Bui M, et al. Increased ER-mitochondrial coupling promotes mitochondrial respiration and bioenergetics during early phases of ER stress. J Cell Sci. 2011;124(Pt 13):2143-52.

80. Dematteis G, Tapella L, Casali C, Talmon M, Tonelli E, Reano S, et al. ER-mitochondria distance is a critical parameter for efficient mitochondrial Ca(2+) uptake and oxidative metabolism. Commun Biol. 2024;7(1):1294.
81. Fernandes T, Domingues MR, Moreira PI, Pereira CF. A Perspective on the Link between Mitochondria-Associated Membranes (MAMs) and Lipid Droplets Metabolism in Neurodegenerative Diseases. Biology (Basel). 2023;12(3).
82. Silva A, Prior R, D'Antonio M, Swinnen JV, Van Den Bosch L. Lipid metabolism alterations in peripheral neuropathies. Neuron. 2025;113(16):2556-81.
83. Ranieri M, Brajkovic S, Riboldi G, Ronchi D, Rizzo F, Bresolin N, et al. Mitochondrial fusion proteins and human diseases. Neurol Res Int. 2013;2013:293893.
84. Wang S, Sang X, Li S, Yang W, Wang S, Chen H, Lu C. Author Correction: Increased Ca2+ transport across the mitochondria-associated membranes by Mfn2 inhibiting endoplasmic reticulum stress in ischemia/reperfusion kidney injury. Sci Rep. 2024;14(1):2478.
85. Lv Y, Chen L, Li L, Liao Z, Fang Z, Cheng L, Peng F. The structure and function of mitofusin 2 and its role in cardiovascular disease through mediating mitochondria-associated endoplasmic reticulum membranes. Front Cardiovasc Med. 2025;12:1535401.
86. Soldner F, Laganiere J, Cheng AW, Hockemeyer D, Gao Q, Alagappan R, et al. Generation of isogenic pluripotent stem cells differing exclusively at two early onset Parkinson point mutations. Cell. 2011;146(2):318-31.
AI-assisted writing support (GenAI) was used for language refinement.

Acknowledgements
This thesis would not have been completed without the contributions of various persons and research groups. I am deeply grateful to the research group of Prof. Dr. Esther Wolfs of the Functional Imaging & Research On Stem Cells (FIERCE) and the research group of Prof. Dr. Ivo Lambrichts of Histology and Regeneration (HISTOREGEN), department at the Biomedical Research Institute (BIOMED, UHasselt) for their educational investment, guidance, assistance, and effort during my senior internship. I am especially grateful for the guidance of my daily supervisors, Hanne Jeurissen and Karen Libberecht. I would like to thank them for their guidance in academic research, for teaching me experimental techniques, for providing valuable scientific insights, and for continuously challenging me to think critically. I also deeply appreciate their support, trust, and invaluable feedback on both my thesis and my experimental work throughout this internship. Furthermore, I would like to thank them for always being willing to answer questions and discuss results. Finally, I would like to thank my family and friends for their support, encouragement, and understanding throughout this internship and the writing of this thesis.

Author contributions
Prof. Dr. Esther Wolfs and Prof. Dr. Ivo Lambrichts conceived and designed the experimental approach of my thesis. Hanne Jeurissen and Karen Libberecht supervised the study, with guidance in daily planning, experimental procedures, data analysis, and thesis writing. Kiara De Cauwer conducted the daily experiments, analyzed the obtained data, and worked on the daily planning, with the valuable feedback and assistance of Hanne Jeurissen and Karen Libberecht. The thapsigargin experiments were conducted by Kiara De Cauwer following an in-house protocol from the research group Molecular and Cellular Signal Transduction. The Seahorse metabolic measurements were conducted by Thomas Raps. Hanne Jeurissen performed immunocytochemistry for CNX, CRT, and TOM20, while Kiara De Cauwer conducted the subsequent microscopy and data analysis. Kiara De Cauwer wrote this thesis with valuable feedback and edits from Karen Libberecht and Hanne Jeurissen.

Supplementary

List of abbreviations

ATF6, Transcription Factor 4; **ATF6**, Transcription Factor 6; **ATP**, Adenosine triphosphate; **BAX**, Bcl-2–Associated X Protein; **BCA**, Bicinchoninic Acid; **BCL2**, B-cell Lymphoma 2; **BiP**, Binding Immunoglobulin Protein; **BSA**, Bovine Serum Albumin; **Ca^{2+}**, Calcium; **cDNA**, complementary deoxyribonucleic acid; **CHOP,** C/EBP Homologous Protein; **CNX,** Calnexin; **CRT,** Calreticulin; **CMT**: Charcot-Marie-Tooth disease; **CMT1A**, Charcot-Marie-Tooth type 1A; **DMEM**, Dulbecco's Modified Eagle Medium; **ER**, Endoplasmic Reticulum; **EDEM**, ER Degradation-Enhancing α-Mannosidase–Like Protein; **eIF2α**, Eukaryotic Initiation Factor 2 Alpha; **ErbB2/ErbB3,** ErbB2 Receptor Tyrosine Kinase/ErbB3 Receptor Tyrosine Kinase; **ERAD**, ER-Associated Degradation; **FAS**, Fas Cell Surface Death Receptor; **FCCP**, Carbonyl Cyanide-p-Trifluoromethoxyphenylhydrazone; **ICC**, Immunocytochemistry; **GADD34**, Growth Arrest and DNA Damage–Inducible Protein 34; **GAPDH**, Glyceraldehyde-3-phosphate dehydrogenase; **GFR**, Growth Factor Reduced; **GRP94**, Glucose-Regulated Protein 94; **hBSA**, High Bovine Serum Albumin treatment; **HRP**, Horseradish Peroxidase; **IRE1α**, Inositol-Requiring Enzyme 1 Alpha; **IP3R**, ER Inositol 1,4,5-trisphosphate receptor; **iPSC**, Induced Pluripotent Stem Cell; **ISO**, Isogenic Control; **iSC**, Immature Schwann Cell; **MAM**, Mitochondria-Associated Membrane; **MERC**, Mitochondria–Endoplasmic Reticulum Contact Site; **MFN1**, Mitofusin 1; **MFN2**, Mitofusin 2; **MPZ,** Myelin Protein Zero; **NCV**, Nerve Conduction Velocity; **mRNA**, Messenger Ribonucleic Acid. **NRG1**, Neuroregulin-1; **OCR**, Oxygen Consumption Rate; **OMM**, Outer Mitochondrial Membrane; **PCR**, Polymerase Chain Reaction; **PDI,** Protein Disulfide Isomerase; **p-eIF2α**, Phosphorylated Eukaryotic Initiation Factor 2 Alpha; **Pen/Strep**, Penicillin/Streptomycin; **PERK**, Protein kinase RNA-like endoplasmic reticulum kinase; **PFA**, Paraformaldehyde; **PMP22**, Peripheral Myelin Protein 22; **PNS**, Peripheral Nervous System; **PVDF**, Polyvinylidene Fluoride; **qPCR**, Quantitative Polymerase Chain Reaction; **RIPA**, Radioimmunoprecipitation Assay**; RNA**, Ribonucleic Acid; **Rot/AA**, Rotenone/Antimycin A; **RPL13**, Ribosomal Protein L13; **SC**, Schwann Cell, **SCP**, Schwann Cell Precursor; **SERCA**, Sarco/Endoplasmic Reticulum Ca^{2+}-ATPase; **SEM**, Standard Error of the Mean; **sXBP1**, Spliced X-box Binding Protein 1; **TEM**, Transmission Electron Microscopy; **TG**, Thapsigargin; **TOM20**, Translocase of the Outer Mitochondrial Membrane 20; **UPR**, Unfolded Protein Response; **VDAC**, Voltage-Dependent Anion Channel; **WB**, Western Blot; **XBP1**, X-box Binding Protein 1; **YWHAZ**, Tyrosine 3-Monooxygenase /Tryptophan 5-Monooxygenase Activation Protein Zeta

Supplementary methods:

High BSA treatment –iPSC-derived SCPs were seeded at a density of $2x10^5$ cells. Prior to harvesting, iPSC-derived SCPs were treated with 0.5% BSA, diluted in SCP medium, for 48 h.

iSC differentiation - For further differentiation of SCPs into iSCs, the protocol established by Prior. et al. (8) was followed. At day 27, starting from iPSC differentiation towards SCPs, SCPs were seeded at a density of $2x10^5$ cells onto 100 µg/mL Poly-L-ornithine (Sigma-Aldrich, St. Louis, MO, USA) and 5 µg/mL Laminin (Sigma-Aldrich, St. Louis, MO, USA)-coated 6-well plates containing complete SCP medium. At day 28, SCP medium was replaced with iSC induction medium containing DMEM-F12 enriched with 100 U/mL Pen/Strep, 40 µM SB431542, 6 µM Chir99021, 200 nM Retinoic acid (ThermoFisher Scientific), 20 ng/mL platelet-derived growth factor-BB (PDGF-BB) (Immunotools, Friesoythen, Germany), 5 µM forskolin (Stemcell Technologies, Vancouver, BC, Canada), and 200 ng/mL NRG-1. After two days, the medium was replaced with iSC differentiation medium consisting of 1:4 DMEM-F12 and DMEM-F12 high glucose supplemented with 100 U/mL Pen/Strep, 0.005% BSA, 20 µM SB431542, 3 µM Chir99021, 100 nM Retinoic acid, 10 ng/mL PDGF-BB, 5 µM forskolin, and 200 ng/mL NRG-1. At day 32, cells were cultured in final iSC medium containing DMEM-F12, 100 U/mL Pen/Strep, 0.005% BSA, 5 µM forskolin, and 200 ng/mL NRG1, at 37 °C in a humidified incubator with 5% CO_2 until further use. The medium was refreshed every two days. The absence of mycoplasma contamination was routinely checked.

Supplementary tables:

Supplementary Table 1 – Growth factors in SCP differentiation medium

Growth factor	Concentration	Company
Bovine Serum Albumin	0.005%	Avantor™, France
Glutamax	2 mM	ThermoFisher Scientific
Pen/Strep		ThermoFisher Scientific
N-2 supplement	100X	ThermoFisher Scientific
B-27 supplement without vitamin A	1X	ThermoFisher Scientific
SB431542	20 µM	Tocris, Abingdon, United Kingdom
Chir99021	3 µM	Tocris, Abingdon, United Kingdom

Supplementary Table 2 – *Primer sequences*

Gene of interest	**Associated UPR pathway/function**	**Primer pair**
ATF4	PERK-signaling	Forward primer 5′–3′: CTCCAACAACAGCAAGGAGGA Reverse primer 5′–3′ : ATACCCAACAGGGCATCCAA
ATF6	ATF6-signaling	Forward primer 5′–3′: ACTATGGACCTATGAGCATGTTGG Reverse primer 5′–3′: GTGTCCTGTGCCTCTTTAGCA
BAX	Pro-apoptotic signaling	Forward primer 5′–3′: GCCCTTTTGCTTCAGGGTTTC Reverse primer 5′–3′: TGAGACACTCGCTCAGCTTC
BiP	ER-chaperone / UPR regulator	Forward primer 5′–3′: GAGGTGGGCAAACAAAGA Reverse primer 5′–3′: ACAACTGCATGGGTAACCTTCT
BCL2	Anti-apoptotic signaling	Forward primer 5′–3′: GGATAACGGAGGCTGGGATG Reverse primer 5′–3′: GTCTTCAGAGACAGCCAGGAG
CHOP	ER-stress-induced apoptosis	Forward primer 5′–3′: CCTCCTGGAAATGAAGAGGAAGA Reverse primer 5′–3′: GTGACCTCTGCTGGTTCTGG
CNX	ER-chaperone	Forward primer 5′–3′: GCTGGTTAGATGATGAGCCTGAG Reverse primer 5′–3′: ACACCACATCCAGGAGCTGACT
CRT	ER-chaperone	Forward primer 5′–3′: ACAACTTCCTCATCACCAACGA Reverse primer 5′–3′: TTGTTTCTCTGCTGCCTTTGTT
EDEM	ER-associated degradation	Forward primer 5′–3′: ACACCTGGGGCAGTTTTTCT Reverse primer 5′–3′: TGGAGCACTTCAACCACTCTT
FAS	Pro-apoptotic signaling	Forward primer 5′–3′: GACCCTCCTACCTCTGGTTCTT Reverse primer 5′–3′: ACAGTCTTCCTCAATTCCAATCC
GRP94	ER chaperone / protein folding	Forward primer 5′–3′: GAGAGTCGTGAAGCAGTTGAG Reverse primer 5′–3′: CCACAGCCTTTTCAATCTTGTCC
GADD34	PERK-signaling	Forward primer 5′–3′: GACTGCAAAGGCGGCTCAA Reverse primer 5′–3′: GGAGAAGCGCACCTTTCTGG
IRE1α	IRE1α-signaling	Forward primer 5′–3′: CCGGCCTCGGGATTTTTGG Reverse primer 5′–3′: GATTGAGCCTGTCCTCTTGCT
PDI	ER folding	Forward primer 5′–3′: CCTGGAGGAGGAGATGACCAA Reverse primer 5′–3′: GCTCATCAGGTGGGGCTTG
PMP22	CMT1A-associated gene	Forward primer 5′–3′: TGGTGATGATGAGAAACAGT Reverse primer 5′–3′: TGATTCTCTCTAGCAATGGA
sXBP1	IRE1α-signaling	Forward primer 5′–3′: GAAGGCGCTGAGGAGGAAAC Reverse primer 5′–3′: TTCTAAATCTACCACTTGCTGTTCC

GAPDH	Housekeeping gene	Forward primer: GAGTCAACGGATTTGGTCGT Reverse primer 5'-3': GACAAGCTTCCCGTTCTCAG
RPL13	Housekeeping gene	Forward primer 5′–3′: AAGTTGAAGTACCTGGCTTTCC Reverse primer 5′–3′: GCCGTCAAACACCTTGAGAC
YWHAZZ	Housekeeping gene	Forward primer 5′–3′: GAGTCAACGGATTTGGTCGT Reverse primer 5′–3′: GACAAGCTTCCCGTTCTCAG

Supplementary Table 3– Primary and secondary antibodies

A) Primary antibodies

Target protein	**Clonality**	**Host species**	**Company**	**Cat.no**	**Application/ dilution**	**Diluted in**
GRP78 (BiP)	Polyclonal	Rabbit	ProteinTech	11587-1-AP	WB (1:1000)	3% BSA
EiF2α	Monoclonal	Rabbit	Cell Signalling	5324T	WB (1:2000)	3% BSA
P-EiF2α	Monoclonal	Rabbit	Cell Signalling	3398T	WB (1:2000)	3% BSA
XBP1s	Monoclonal	Rabbit	Cell signaling	40435s	WB (1:1000)	3% BSA
GAPDH	Monoclonal	Mouse	Santa Cruz	SC 32233	WB (1:3000)	3% BSA
MFN2	Monoclonal	Rabbit	Cell signaling	D2D10	ICC (1:300), 555nM	PBS-10% DAKO
CNX	Polyclonal	Rabbit	Abcam	22595	ICC (1:400)	PBS-10% DAKO
CRT	Polyclonal	Rabbit	Proteintech	27298-1-AP	ICC (1:250)	PBS-10% DAKO
TOM20	Monoclonal	Mouse	Proteintech	66777-1-IG	ICC (1:400)	PBS-10% DAKO

B) Secondary antibodies

Target species	Wavelength	Host species	Company	Cat.no	Application/ dilution	Diluted in
Anti-Rabit	555	Goat	Invitrogen	A21428	ICC (1:400)	PBS
Anti-Mouse	647	Goat	Invitrogen	A21235	ICC (1;400)	PBS
Anti-Rabit	/	Goat	ThermoFisher Scientific	41798650	WB (1:2000)	3% BSA
Anti-Mouse	/	Rabbit	ThermoFisher Scientific	41784664	WB (1:2000)	3% BSA

Supplementary figures

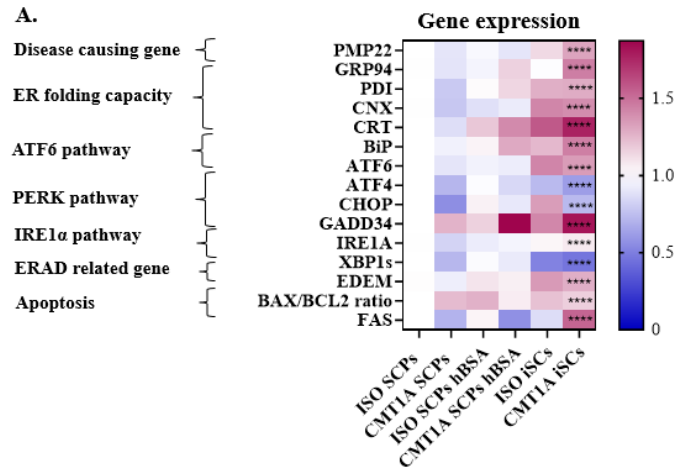

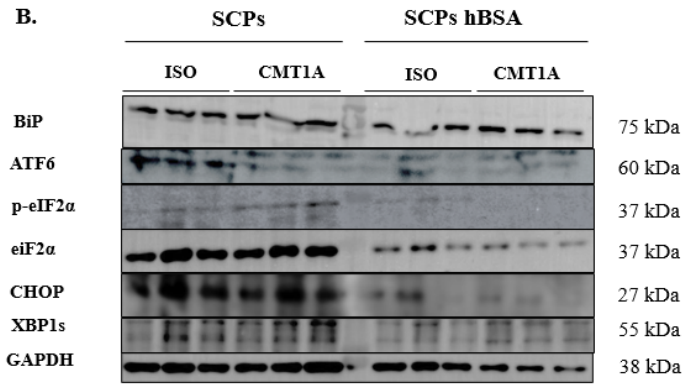

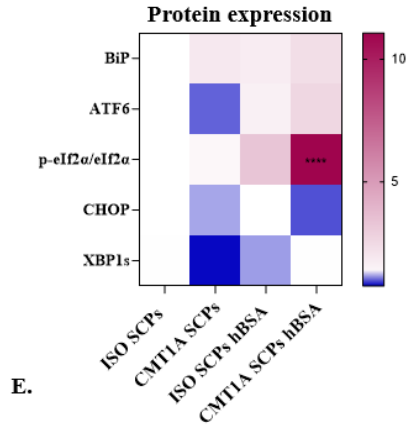

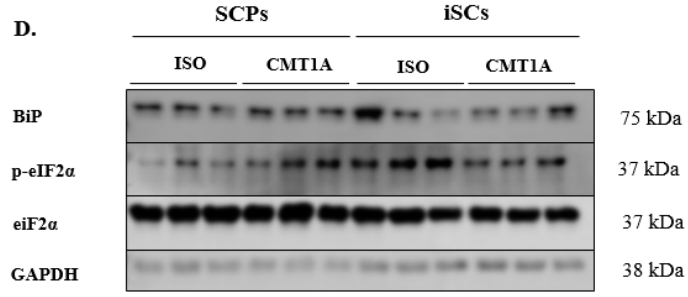

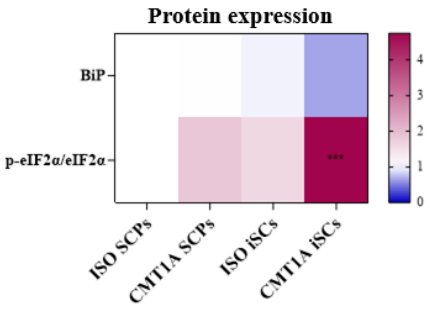

Supplementary Figure 1. – Basal UPR-related expression is largely unaffected by hBSA treatment in isogenic control and CMT1A SCPs or maturation towards iSCs. A. Heatmap showing the relative expression of UPR-related genes under basal conditions in untreated ISO and CMT1A SCPs (n=4), as well as in corresponding hBSA-treated conditions (n=3) and iSCs (n=3), normalized to untreated isogenic SCPs. Additionally, no significant differences were observed between isogenic and CMT1A iSCs, nor between hBSA-treated isogenic and CMT1A SCPs. **B-C**. Representative Western blots of UPR-related proteins and quantification in untreated and hBSA-treated isogenic control and CMT1A SCPs (**B** and **D**), or isogenic control and CMT1A SCPs together with iSCs (**C** and **E**), normalised to isogenic control SCPs (n=3). Black asterisks indicate statistically significant differences between CMT1A SCPs and CMT1A iSCs. Data are presented as mean ± SEM. Statistical analysis was performed using a 2-way ANOVA with Šídák's multiple comparisons test. *p < 0.05, **p < 0.01, ****p < 0.001.

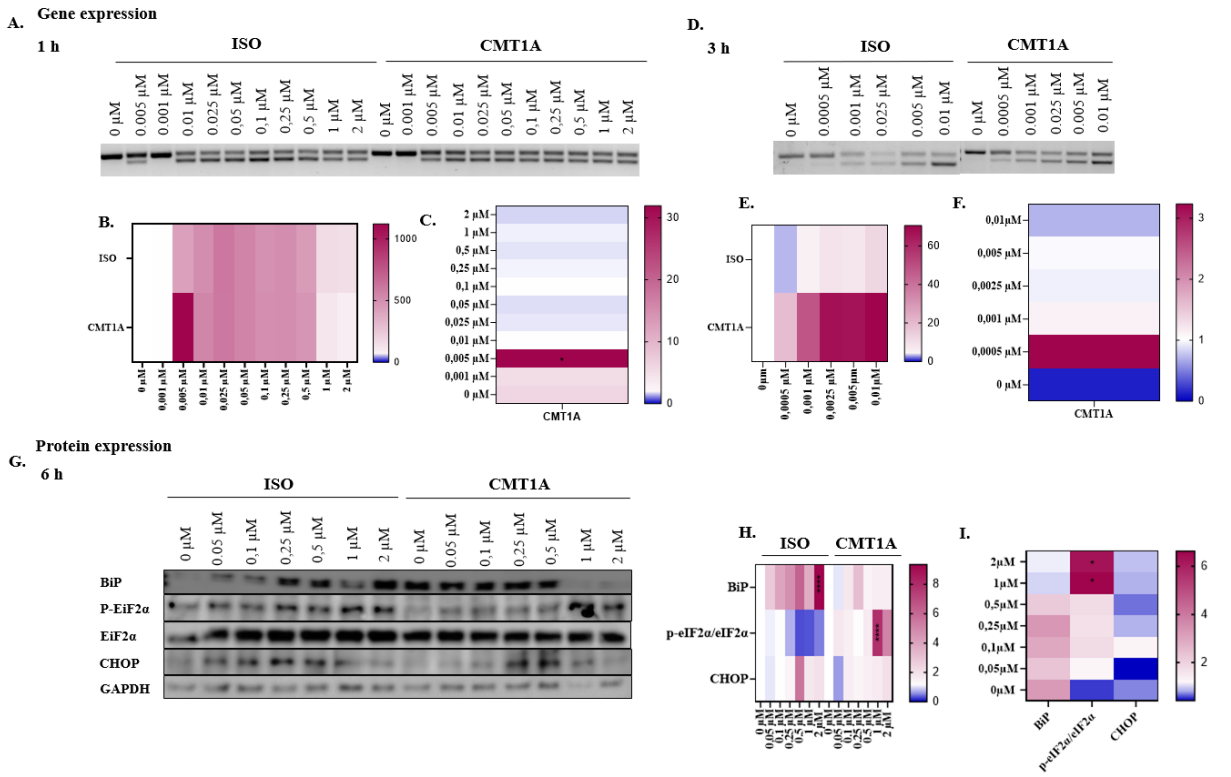

Supplementary Figure 2. – Dose-response to experimentally induced ER stress following stimulation with increasing concentrations of thapsigargin for 1 h, 3 h, and 6 h in isogenic control and CMT1A SCPs. A-C. Representative RT-PCR image and quantification of XBP1-splicing in isogenic and CMT1A SCPs normalized to GAPDH expression and relative to the corresponding basal condition (**B**), or each isogenic control concentration (**C**), after 1 h stimulation with increasing TG concentrations (n=3). **D.** Representative RT-PCR image and quantification of XBP1-splicing in isogenic control and CMT1A SCPs, normalized to GAPDH expression and relative to the corresponding basal condition (**E**), or each isogenic control concentration (**F**) after 3 h stimulation with increasing TG concentrations (n=1). **G.** Representative Western blot images of ER-stress related proteins following 6 h TG stimulation at increasing concentrations and quantification of the relative protein expression compared to each basal condition (**H**) or isogenic controls at each TG concentration (**I**) in isogenic control and CMT1A SCPs (n=3-4). Data are presented as mean ± SEM. Statistical analysis was performed using a 2-way ANOVA with Šídák's multiple comparisons test. n=3. *p < 0.05, **p < 0.01, ***p < 0.001.